Curry, W.B., Shackleton, N.J., Richter, C., et al., 1995
Proceedings of the Ocean Drilling Program, Initial Reports, Vol. 154

9. LEG 154 SYNTHESIS[1]

Shipboard Scientific Party[2]

INTRODUCTION

One of the major objectives of the Ocean Drilling Program is to recover sedimentary sections that will enable us to reconstruct the history of global climate and ocean circulation with sufficient detail that we can understand the causes of climatic change. Many recent syntheses have emphasized the fact that the geological record of climatic change consistently documents variability both on a time scale of 10^4 to 10^5 yr and on time scales of 10^6 yr and upward. The higher frequency variability is very confidently associated with changes in Earth-sun orbital geometry, at least over the last few million years, and is referred to as "orbital scale variability." Variability on longer time scales probably has a wider range of causes, although each of these may ultimately be attributed to tectonic processes. Over the interval of time covered by the sediments recovered during Leg 154, the Atlantic Ocean has widened considerably; the passages at both the northern and southern ends have changed beyond recognition; the connection with the Pacific in tropical latitudes has closed. At the same time, there have been global changes in sea level and major episodes of mountain building and volcanism, which may have had significant effects on atmospheric circulation and chemistry. Understanding the operation of these multiple causes is a gradual process, but it can be accelerated by conducting well-planned drilling operations in carefully selected regions. Leg 154 was planned with the idea that, at the present state of our understanding, we need to gain a better understanding of the history of the vertical physical and chemical structure of the oceans in both high and low latitudes. In addition, new information is critically needed on the history of the surface temperature and chemical character (especially pCO_2) of the warmest regions of the ocean.

The Ceara Rise has several features that made it a particularly attractive target for an ODP paleoceanographic drilling leg. It has a sedimentary drape over a water-depth range that encompasses the deep-water masses of the present and last glacial ocean. The deep-water mass structure is not complicated by deep sills as it is in the eastern Atlantic Ocean. The overlying surface waters may be described as "warm surface water" in both physical (a small seasonal range) and chemical senses in that it has a low nutrient content (Broecker, 1982), yet the terrigenous input from the Amazon River generates a much higher sedimentation rate than is usual under such surface-water masses. Piston cores taken during the site-survey cruise as well as on previous expeditions demonstrate sedimentation rates of up to 5 cm/k.y. (50 m/m.y.). Spot coring at DSDP Site 354 had indicated that the sediments contained the well-preserved carbonate microfossils that are necessary for detailed paleochemical work (Biolzi, 1985). Detailed surveys indicated that it would be possible to recover undisturbed sedimentary records over a wide range of water depths.

Two additional features render a drilling cruise on the Ceara Rise a timely endeavor. First, the opportunity to obtain a long record of the output of the Amazon River offers the possibility of gaining critical information with regard to the history of the major area of present-day tropical rain forest as well as the uplift history of the Andes. Second, the recent completion of investigations in the eastern tropical Pacific (Mayer, Pisias, Janecek, et al., 1992; Pisias, Mayer, Janecek, Palmer-Julson, and van Andel, 1994) provides the basis for a new level in our understanding of the history of the Pacific-Atlantic connection across Central America and its role in controlling ocean circulation.

Figure 1 shows the location of the sites drilled during Leg 154. The primary objectives of the shipboard operations were to recover the targeted sedimentary sequences; to document continuity in the recovered sequences over at least the whole of the late Neogene; to recover sufficient material that the post-cruise science would not be hampered by lack of material; and to complete those phases of the analysis of the sediments that can only be performed on unsplit core sections, or can only be efficiently completed aboard ship. Of necessity, this means that this volume contains documentation of a huge number of routine yet extremely valuable observations. In this chapter, we attempt to synthesize these observations while recognizing that because the objectives of the shipboard operations are so limited, the chief value of the synthesis is to provide the framework for the post-cruise investigations.

LITHOSTRATIGRAPHY

The sediments cored at five sites along the Ceara Rise depth transect are predominantly pelagic oozes, clays, chalks, claystones, and limestones. Calcareous nannofossils, foraminifers, and clay minerals are the primary constituents. The sections are biostratigraphically complete except for a few hiatuses that add up to no more than a few million years of missing record, identified at different stratigraphic levels at different sites. Three lithostratigraphic units (and a series of subunits) were recognized at each site (Fig. 2). The units were defined on the basis of changes in the same set of lithologic characteristics: (1) carbonate content, (2) percentage color reflectance, and (3) magnetic susceptibility. Downcore variations in lithology at each site mainly reflect changes in the relative fluxes of biogenic and terrigenous sediments over the Cenozoic, as influenced by regional productivity and the late Neogene uplift of the Andes and growth of the Amazon fan. Differences in unit lithology among the sites mainly reflect variations in the preservation of biogenic calcite and opal and redox conditions in response to changes in deep-water chemistry and circulation patterns. Some of the most prominent features of sediment deposition at the Ceara Rise include (1) decimeter- to meter-scale cyclic variability within Ceara Rise sediments throughout the entire Cenozoic in the form of distinct changes in sediment color and composition; (2) progressive thinning of in-place sediments within lithostratigraphic units (and subunits) with increasing water depth in response to the prevailing carbonate dissolution gradient; (3) discrete episodes of significant biogenic silica accumulation in the early Oligocene and early Miocene; (4) a gradual increase in clay accumulation rates over the Pliocene–Pleistocene; (5) a rapid shift from low to high illite/kaolinite ratios in the late Miocene; and (6) sediment slumping and turbidity current deposition within distinct time intervals from the middle Eocene to latest Miocene. Specific aspects of these features are discussed below.

[1] Curry, W.B., Shackleton, N.J., Richter, C., et al., 1995. *Proc. ODP, Init. Repts.,* 154: College Station, TX (Ocean Drilling Program).

[2] Shipboard Scientific Party is as given in the list of participants preceding the contents.

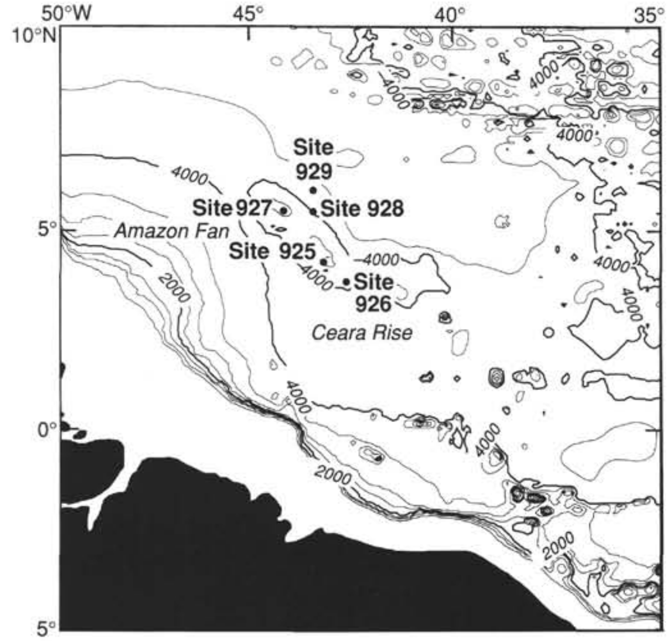

Figure 1. Location of Leg 154 sites.

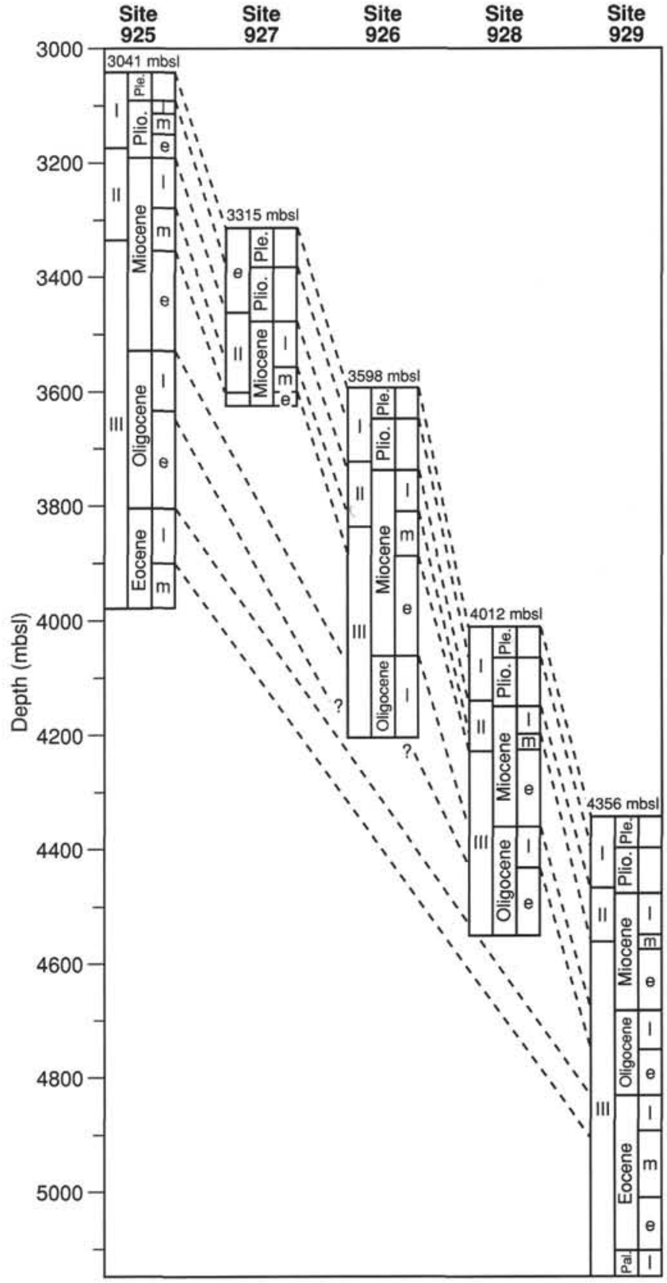

Figure 2. Primary lithostratigraphic units (left, labeled I, II, and III) and ages of sediments for each of the Leg 154 sites. The sediments are shown at their present depths below sea level (mbsl).

Carbonate Content Proxies

Calcareous microfossils constitute significant fractions of almost all Ceara Rise sediments, and the bulk carbonate content of these sediments varies widely. Some bulk sediment properties reflect this variation in carbonate content. Three parameters—percentage of color reflectance (550 nm), magnetic susceptibility, and natural gamma emissions—were examined to determine how closely they covary with carbonate content (Fig. 3) at low resolution over the entire sedimentary sequence. Simple linear regressions were derived to estimate carbonate content from color reflectance, magnetic susceptibility, and natural gamma data for each unit (I–III) and each site (925–929); the model parameters (slope, intercept, and R^2) are given in Table 1.

Percentage of color reflectance correlates positively with carbonate content in all cases except at Site 927, Unit III, for which only eight carbonate measurements were available. This is expected because calcium carbonate is more reflective than the terrigenous materials that make up most of the noncarbonate fraction of the Ceara Rise sediments. Figure 3A indicates that the relationship between carbonate and reflectance is nonlinear, especially for Unit II. The wide variability in slopes (Table 1) for color reflectance–carbonate regressions also indicates a nonlinear relationship caused by heterogeneity in the color of the terrigenous materials and diagenesis of mineral phases.

Magnetic susceptibility shows a strong negative correlation with carbonate in Unit II and, to a lesser extent, in Unit I (Fig. 3B and Table 1). These units are relatively rich in iron oxides and oxyhydroxides, materials that are highly susceptible to an induced magnetic field. The correlation in Unit III, though stronger than for other bulk sediment proxies ($R^2 = 0.51$), represents very low overall values rather than any strong predictive correlation. This implies that any iron in Unit III sediments is in paramagnetic phases that are not strongly susceptible to magnetic fields.

Natural gamma emissions reflecting the presence of radioactive elements in clay minerals also negatively correlates with carbonate content. The slope of the natural gamma–carbonate regression is very constant among units and sites (Table 1), but the values show much more scatter than other proxies (Fig. 3C). Thus, the natural gamma measurements reflect carbonate content in a more consistent way than the other measurements, but with less precision for a single estimate.

Cenozoic Lithostratigraphy and Cyclostratigraphy from Visible Light Reflectance

The color reflectance, magnetic susceptibility, and natural gamma records can be used as proxies for both long- and short-term changes in sediment carbonate content. Because these proxies were measured every 3–10 cm (whereas carbonate content was measured roughly every 3 m), they are more suitable for reconstructing high-frequency changes in carbonate sedimentation. The lower signal-to-noise ratio for natural gamma makes it less suitable than the other parameters; furthermore, in parts of the records at all sites, the magnetic susceptibility signal is also very weak. However, nearly every core from each of the Leg 154 sites exhibited centimeter- to decimeter-scale cyclic

Table 1. Parameters of linear regression of percentage of color reflectance, magnetic susceptibility, and natural gamma emission on calcium carbonate contents, arranged by site and lithologic unit.

	Unit I			Unit II			Unit III			All units		
	Reflectance (%)	Magnetic susceptibility	Natural gamma	Reflectance (%)	Magnetic susceptibility	Natural gamma	Reflectance (%)	Magnetic susceptibility	Natural gamma	Reflectance (%)	Magnetic susceptibility	Natural gamma
Site 925:												
Slope	0.30	−0.32	−0.25	0.67	−0.39	−0.30	0.24	−0.13	−0.09	0.37	−0.28	−0.18
Intercept	8.03	33.43	36.65	−14.88	37.98	41.37	17.64	13.40	23.74	7.03	27.65	31.92
R^2	0.75	0.72	0.78	0.58	0.74	0.56	0.41	0.35	0.30	0.57	0.47	0.50
Site 926:												
Slope	0.27	−0.38	−0.19	0.43	−0.41	−0.24	0.36	−0.14	−0.20	0.41	−0.30	−0.20
Intercept	8.57	36.32	30.08	2.26	40.18	33.45	11.30	14.77	29.56	5.84	28.16	30.45
R^2	0.83	0.74	0.81	0.52	0.66	0.49	0.67	0.55	0.65	0.64	0.45	0.67
Site 927:												
Slope	0.22	−0.41	−0.23	0.52	−0.39	−0.20	−0.26	−0.18	−0.22	0.39	−0.44	−0.23
Intercept	13.01	39.28	32.46	−0.61	36.83	30.81	56.36	17.70	30.33	6.25	40.48	32.61
R^2	0.77	0.41	0.69	0.40	0.51	0.39	0.31	0.48	0.58	0.70	0.68	0.78
Hole 928:												
Slope	0.20	−0.37	−0.20	0.26	−0.47	−0.22	0.39	−0.15	−0.14	0.40	−0.39	−0.21
Intercept	15.89	34.24	31.05	16.95	42.92	34.28	12.91	14.89	25.69	10.66	32.84	31.07
R^2	0.76	0.48	0.57	0.51	0.74	0.64	0.53	0.51	0.41	0.66	0.60	0.62
Hole 929:												
Slope	0.18	−0.37	−0.17	0.19	−0.33	−0.25	0.45	−0.16	−0.18	0.39	−0.40	−0.26
Intercept	17.44	35.31	31.23	20.67	33.51	34.58	12.07	15.99	27.57	13.97	33.56	33.43
R^2	0.72	0.52	0.44	0.45	0.66	0.83	0.74	0.61	0.51	0.72	0.72	0.78
All sites:												
Slope	0.19	−0.36	−0.20	0.25	−0.36	−0.22	0.33	−0.14	−0.16	0.35	−0.35	−0.21
Intercept	14.56	35.39	31.90	15.94	36.21	33.77	15.49	14.83	26.75	11.35	32.07	31.57
R^2	0.58	0.57	0.63	0.40	0.73	0.66	0.46	0.51	0.47	0.55	0.58	0.63

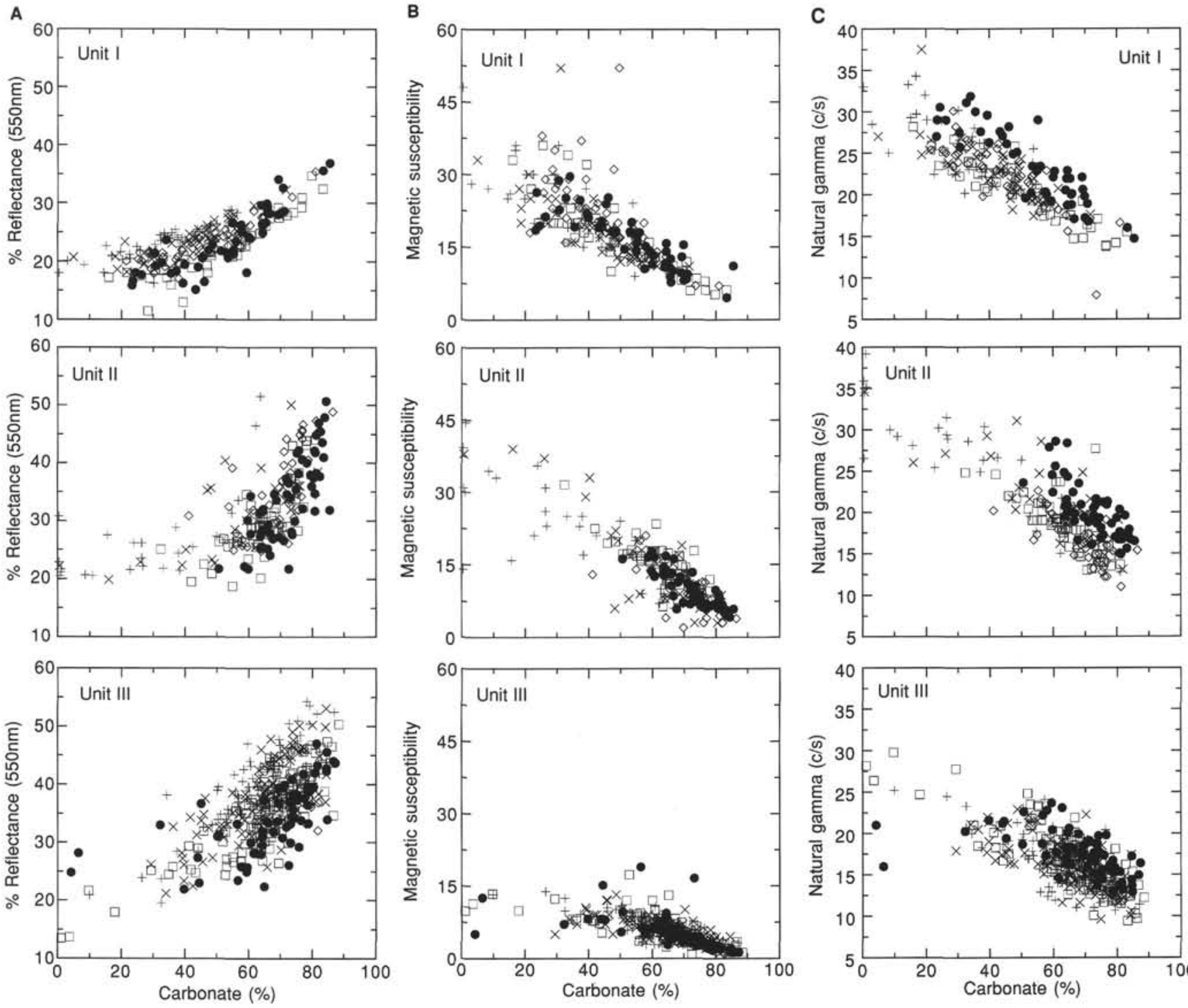

Figure 3. Plots of the relationship between calcium carbonate content and three carbonate-proxy measurements. Site 925 = solid circles, Site 926 = squares, Site 927 = diamonds, Site 928 = x's, and Site 929 = plus signs. **A.** Percentage of color reflectance. **B.** Magnetic susceptibility (machine units). **C.** Natural gamma.

variability in color reflectance (Fig. 4). Spectral analyses of undisturbed intervals indicate that the cycles have orbital scale periods regardless of depth or age (see Fig. 10, "Site 925" chapter, this volume). This implies that much of the short-term variability in carbonate content at the Ceara Rise was controlled by orbitally forced changes in climate and ocean circulation. The amplitude of reflectance cycles decreases from the Miocene to Pleistocene at all sites, and from the shallowest to the deepest sites in the Pliocene–Pleistocene. Both of these trends can be largely attributed to a decline in mean reflectance values caused by a long-term increase in terrigenous clay input, a trend that is enhanced by increasing calcium carbonate dissolution at the deeper sites. Moreover, the lack of a noticeable depth-related difference in the amplitude of cycles in intervals older than the middle Miocene suggests that the water-column carbonate chemistry was comparatively homogeneous over the depth range of the Leg 154 sites during the Paleogene and the early Miocene.

In addition to acting as a proxy for carbonate content, the reflectance data set contains information about other lithologic components and sediment chemistry. The ratio of percentage of reflectance at 700 to 400 nm ("red/blue") reflects the concentration of iron oxides and oxyhydroxides in the sediment and may be partly a proxy for the redox state of iron present. Higher values of the red/blue ratio indicate a greater concentration of iron oxides and oxyhydroxides, which is observed in Unit II at all sites. At Sites 925–928, the red/blue ratio averages close to 1 in Unit III, reflecting the consistently green-colored and reduced sediments of this unit (Fig. 5). At Site 929, the increase in the red/blue ratio begins in sediments from about 18 Ma, rather than from about 12 Ma as it does at the other sites. At Site 929, the ratio varies around unity in sediments older than 18 Ma, as at the other sites. This difference in the oxidation state of iron at Site 929 in the sediments of 18–12 Ma may indicate either (1) a strong vertical dissolved oxygen gradient in deep waters and/or (2) a slightly different early diagenetic history at the deepest site.

Biosiliceous Sedimentation

The Paleogene to Neogene history of sediment deposition at the Ceara Rise is marked by two notable periods of biosiliceous sedimentation and preservation (Fig. 6) in the early Miocene (15–24 Ma) and the early Oligocene (30–35 Ma). Furthermore, there was an enhanced preservation of biosiliceous components with increasing water depth during these two time intervals. Only traces of biosiliceous fragments

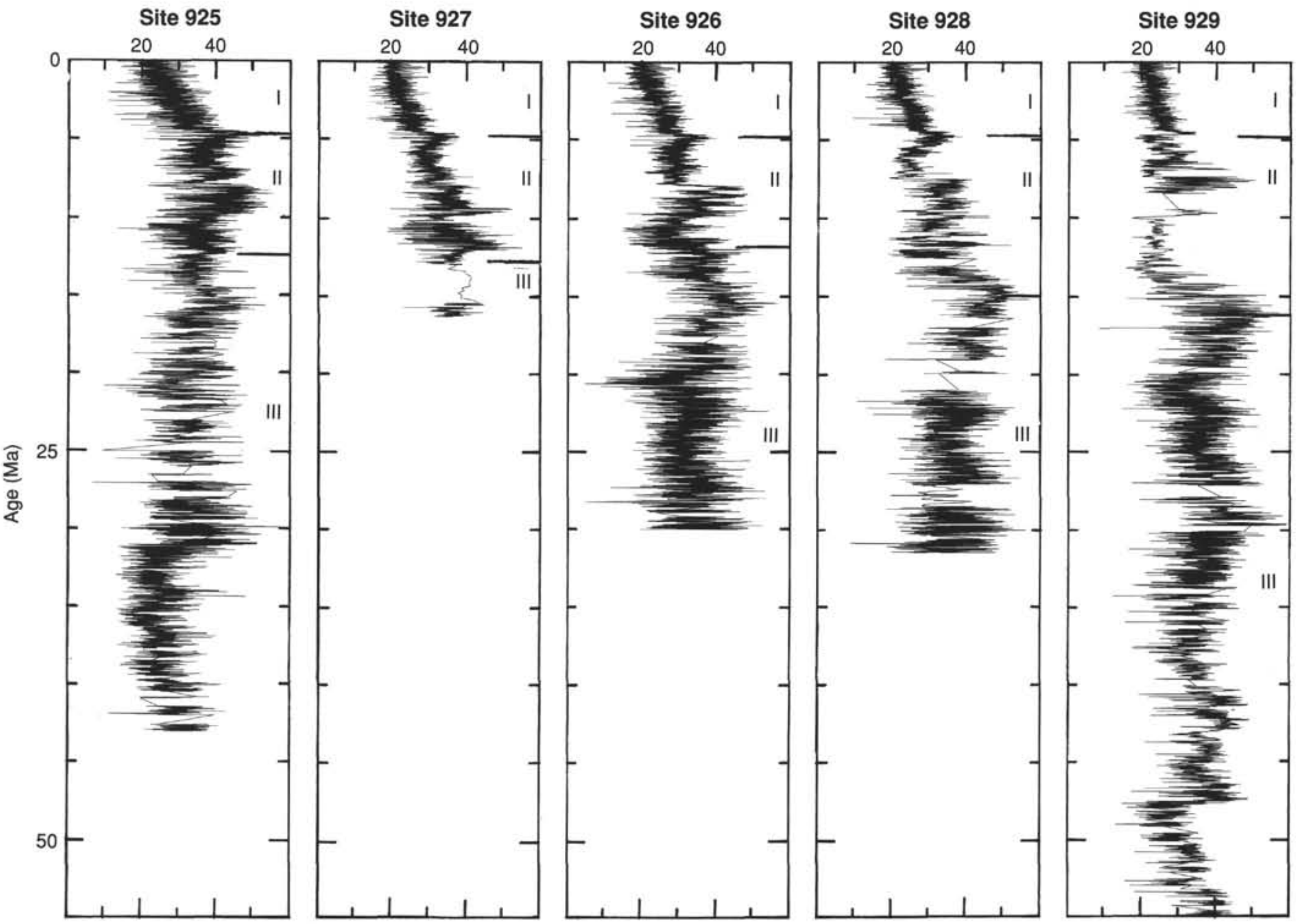

Figure 4. Percentage of color reflectance (550 nm) of sediments at each of the Leg 154 sites vs. age. Measurements were taken at 5-cm intervals. The major lithologic units are shown on the right side of each diagram.

are found at the shallowest site (Site 925). In contrast, the deeper sites exhibit biogenic opal contents of about 5%–15% (estimated in smear slides) for the early Miocene and up to about 30% for the earliest Oligocene at the deepest site (Site 929). Because the supply of biogenic opal from the surface waters was probably about the same at all sites because of their proximity to each other, and because the average carbonate content of the deepest site (Site 929) is only 5%–10% lower than at the shallowest site (Site 925), the occurrence of biogenic opal with increasing water depth is probably related to a gradient in deep-water chemistry (silica solubility) rather than to differences in dilution by carbonate or terrigenous sediment.

The deposition of biogenic opal at the Ceara Rise between 15 and 24 Ma is correlated with the abundance and distribution of Miocene siliceous oozes in the North Atlantic (Keller and Barron, 1983). Additional evidence for enhanced opal concentration in the early Miocene also exists in the eastern equatorial Atlantic Site 667 (Ruddiman et al., 1988). The early Miocene opal deposition at the Ceara Rise might be related to an increase in productivity and/or to changes in deep-water chemistry associated with a reorganization in deep-water circulation patterns.

The sites presently underlie a surface-water mass that is one of the warmest in the world oceans and is characterized by a stable thermocline and low productivity. Sea-surface temperature reconstructions (CLIMAP, 1976) also suggest little variability (<2°C) on glacial to interglacial time scales. An increase in productivity north of the equatorial upwelling zone during the early Miocene would require destratification of the upper water column to allow enhanced upwelling of nutrient-enriched deep waters in the western north equatorial Atlantic, probably associated with an open Isthmus of Panama. However, because the early Miocene preservation event is a widespread feature in the North Atlantic rather than being restricted to upwelling regions, and because it is largely absent in the Pacific and Indian oceans, other factors such as altered basin-to-basin fractionation caused by changes in ocean circulation may have played a more important role. The subsequent decrease in silica preservation in the Atlantic at about 15 Ma has been attributed to the initiation and intensification of North Atlantic Deep Water (NADW) production (Woodruff and Savin, 1989; Wright et al., 1992).

The early Oligocene (32–35 Ma) episode of biosiliceous sedimentation at the Ceara Rise also coincides with a period of significant global climate change. There is considerable evidence for cooling of the high latitudes and deep ocean as well as for rapid growth of large continental ice sheets on Antarctica during the early Oligocene (Miller et al., 1987a; Barrera and Huber, 1991; Stott et al., 1990; Zachos et al., 1992, 1993; Miller et al., 1991; Wise et al., 1991; Barrett et al., 1989). Evidence further suggests that these climatic changes triggered a major reorganization in deep-ocean circulation patterns by intensifying thermohaline circulation and the rate of oceanic overturn (Kennett and Shackleton, 1976). The increase in biosiliceous sedimentation at the Ceara Rise may be a consequence of these changes in deep-ocean circulation. Elevated levels of opal accumulation in the early Oligocene have been documented at some other sites. The most significant increases occurred at low and high latitudes: Site 647 in the Labrador Sea (Bohrmann and Stein, 1989), the eastern equatorial Atlantic (Baldauf

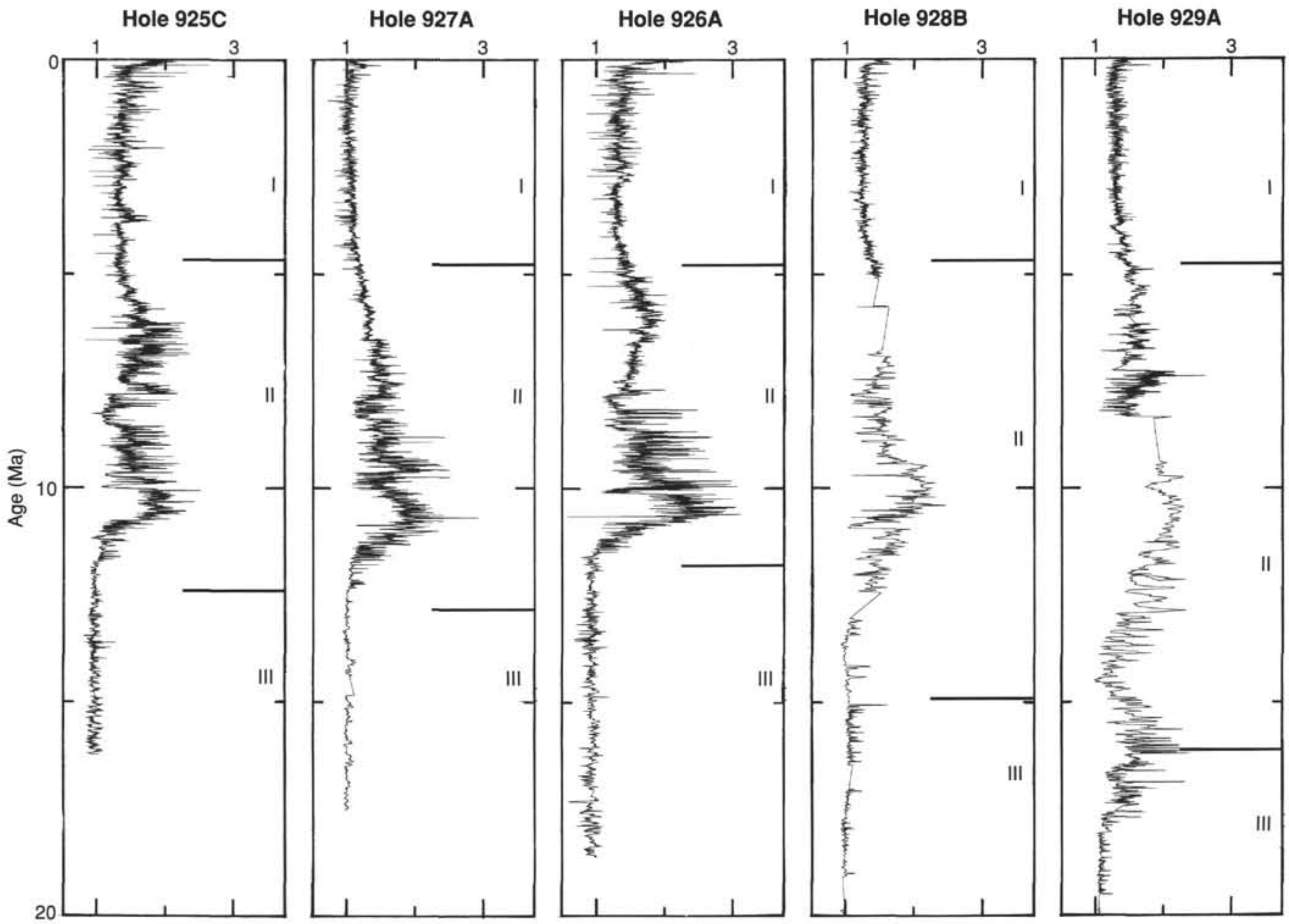

Figure 5. Ratio of percentage of color reflectance at 700 nm (red) to 400 nm (blue) in sediments from each Leg 154 site vs. age.

and Barron, 1990), the eastern Pacific (Shipboard Scientific Party, 1972), and the Atlantic and Indian ocean sectors of the Southern Ocean (Barker, Kennett, et al., 1990; Ciesielski, Kristoffersen, et al., 1988; Schlich, Wise, et al., 1989; Baldauf and Barron, 1990). In contrast, sites located in the mid-latitude South Atlantic such as Site 522 show no trace of biogenic silica deposition in the early Oligocene (Hsü, Labrecque, et al., 1984), and in the western Pacific, the pattern of biogenic opal accumulation may be opposite to that in the Atlantic (e.g., Kroenke, Berger, Janecek, et al., 1991). The increase in opal accumulation in the equatorial and northern Atlantic may indicate that during the early Oligocene, net transport of nutrient-rich deep waters was from the Pacific to the Atlantic. This could imply that most deep-water formation was occurring outside of the Atlantic. Also, the increase in biogenic silica accumulation at the Ceara Rise suggests that, during the early Oligocene, (1) the Ceara Rise was located closer to the equatorial divergence than previously suspected and (2) because of global cooling the intensity of trade winds increased so as to enhance equatorial divergence and upwelling of nutrient-rich, deep-water masses in both the eastern and western Atlantic.

Redeposited Sediments

Redeposited material was encountered sporadically at all sites. Siliciclastic turbidites were encountered only in the Pleistocene of Site 929. Calcareous turbidites and grain flows in centimeter- to meter-scale beds are found at all sites and range in age from middle Eocene to latest Miocene. Slumped material was observed with a similar range in ages from all sites except Site 926. The most significant period of slumping occurred in the middle to late Miocene (Fig. 7). Table 2 gives the intervals of redeposited material.

Slumped intervals up to 20 m thick typically contained thinner beds, which were tilted, contorted, sheared, microfaulted, and, in some cases, exhibited horizontal folds. In some cases, the material consists of intervals of stacked turbidites. It was frequently difficult to distinguish coring disturbance from in-situ deformation. In Hole 927A, one 9-m interval, capped by 3 m of contorted beds, showed no evidence for internal deformation. However, this interval was demonstrated to repeat material encountered 15 m below. Hence, this appears to be an example of mass downslope movement of an internally undeformed block of sediment. At the equivalent composite depth in other holes at this site, the deformation characterizing most slumped intervals was present, indicating that the nature of the deformation varied laterally.

Despite a large proportion (24% by thickness) of slumped material in the middle and upper Miocene of Site 928, a linear sedimentation rate was inferred from multiple biostratigraphic datums. This indicates that the thick slumped intervals at this site are composed of stacks of multiple slumps rather than single events. Site 926 has very little evidence for redeposition of sediments, probably reflecting its isolation from shallower topographic highs. As demonstrated in Figure 7, there is a general correspondence in the times of slumping and calcareous turbidite flows on the Ceara Rise. The main episodes were from the middle Eocene to middle Oligocene (44–29 Ma), the late early Miocene to early middle Miocene (19–15 Ma), and the late early

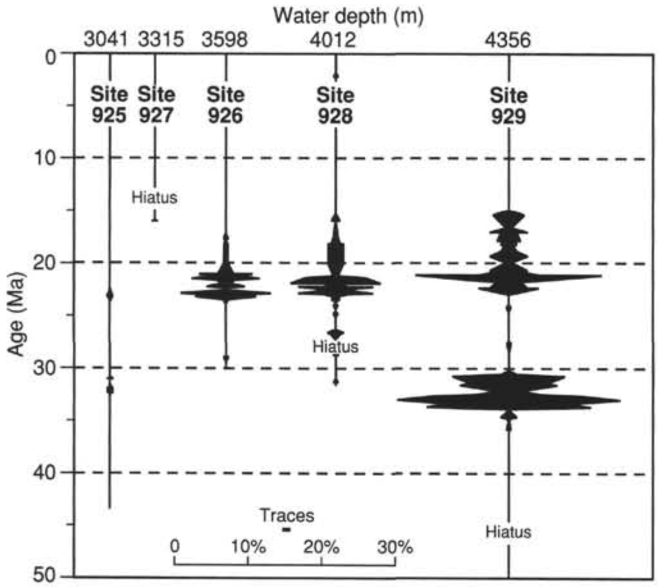

Figure 6. Relative abundance of biosiliceous microfossil fragments (radiolarians and diatoms) at Sites 925 through 929 (3041–4356 m water depth) vs. age. Percentages are based on smear-slide estimates.

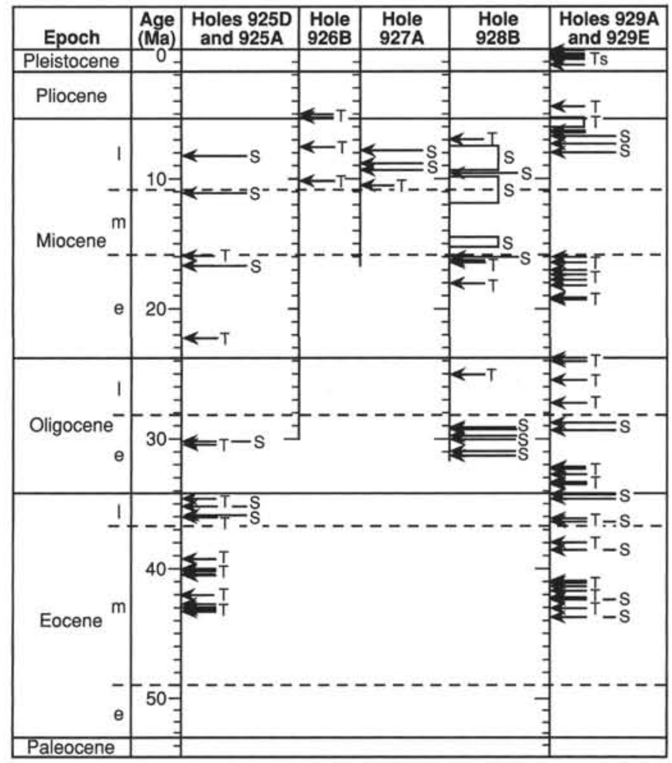

Figure 7. Periods of redeposition of sediment on the Ceara Rise. Arrows indicate discrete events, and brackets indicate periods of multiple events. S = slump, T = calcareous turbidite, and Ts = siliciclastic turbidite.

Miocene to earliest Pliocene (11–4.5 Ma). The coincidence of timing of mass movements at the northern (927, 928, and 929) and southern (925 and 926) sites and the clustering of events in time may possibly indicate that the main trigger for the redeposition events was regional seismic activity.

COMPOSITE SECTION AND SITE-BY-SITE CORRELATION

The use of continuous susceptibility and color reflectance measurements for correlating different sites on the Ceara Rise is based on the presumption that the sedimentary sequence of each site contains similar small-scale variations in both carbonate dissolution and terrigenous sediment supply. The five sites of the depth transect drilled during Leg 154 are located close enough together that one might hope to correlate them with considerable precision. This correlation was achieved through the last 6 m.y. for all sites and was extended to 12 m.y. for the three shallower Sites 925, 926, and 927.

The correlation procedure was based on the availability of a spliced record assembled from the composite section for each site (see "Composite Depth" section in each site chapter), together with a considerable amount of precise biostratigraphic data. The construction of composite sections from Sites 925 through 929 verified that complete recovery of the sedimentary sequence through at least the past 10 m.y. was achieved at every site. At each site, a spliced record of susceptibility, color reflectance, and natural gamma was constructed from the composite sections. These spliced records are continuous, providing the opportunity to correlate between sites at high resolution.

A series of biostratigraphic events was used to provide preliminary control points for correlating the sites; these were taken from the "Sedimentation Rates" section in each site chapter. This provided the basis for an accurate graphic correlation of the susceptibility records of the sites. The detailed correlation was conducted in the depth domain, using Site 926 as the standard. Site 926 was selected as the reference site for correlation because the last 12 m.y. of its sedimentary sequence is the least affected by redepositional events (Table 2). To conduct the correlation, a series of characteristic susceptibility events at intervals of about 5 m was selected. These events were identified at all sites, providing tie-lines between the sites (Table 3). The time scale for Site 926 is interpolated linearly among the small number of biostratigraphic tie-points. In this way, ages were assigned to the correlation tie-points. In Figure 8, the records for Sites 925 and 927–929 are shown on an age scale obtained by using these correlation points to make a detailed correlation to Site 926. The interpolated positions of 38 biostratigraphic datums, as determined on board ship, are shown on Figure 8 for each site and are listed in Table 4. In general, biostratigraphic tie-points are constrained to 1.5 m or closer (corresponding to about 0.05 m.y.); however, it is known that such precision is not meaningful for all datums. In contrast, it is frequently possible to define extreme points or characteristic features in an individual susceptibility cycle in several sites to within 10 cm (corresponding to about 0.003 m.y.). Figure 8 illustrates the precision with which sites on the Ceara Rise can be correlated one to another, and supports the notion that such precise correlations of geological records are indeed valid. In most parts of the sediment sequences, the susceptibility variations of all sites can be correlated to a decimeter scale over all of the last 5.5 m.y. (165 mcd at Site 926). Before 6 Ma, the presence at Sites 928 and 929 of both redeposited sediment and red clay that is barren of calcareous microfossils makes the detailed peak-to-peak correlation impossible for parts of the record at those sites. In addition, the very low variability in susceptibility in the late Miocene interval between 7.5 and 9.5 Ma (200–240 mcd in Site 926) impedes detailed correlation even between the three shallower sites. Nevertheless, a cross-check of the correlation among sites using color reflectance measurements (not shown) provided reliable tie-points for this interval too.

The correlation of sites at such high resolution provides an excellent tool for a refinement of the determination of these biostratigraphic events at each site of the Ceara Rise depth transect. Moreover, the fact that similar correlations were achieved in sediments from the east equatorial Pacific that were drilled during ODP Leg 138 (Raffi and Flores, in press; Shackleton et al., in press) means that the opportunity exists to assess the long-distance synchroneity of biostratigraphic events at a new level of refinement.

Table 2. Locations of turbidite and slump deposits at each of the Leg 154 sites.

Top			Base			
Core, section, interval (cm)	Depth (mbsf)	Depth (mcd)	Core, section, interval (cm)	Depth (mbsf)	Depth (mcd)	Notes
154-925A-						
6R-2, 94	335.54	373.88	6R-2, 100	335.60	373.94	Turbidite
8R-5, 10	358.50	396.84	8R-6, 95	360.85	399.19	Slump
20R-2, 55	469.85	508.19	20R-2, 58	469.88	508.22	Turbidite
39R-6, 98	630.58	668.92	40R-1, 58	661.38	699.99	? Slumped turbidites
42R-1, 0	670.40	708.74	42R-1, 25	670.65	708.99	Turbidite
55R-2, 110	778.60	826.94	55R-2, 115	778.65	826.99	Turbidite
56R-2, 77	797.87	836.43	56R-5, 70	802.30	840.64	Slump
57R-4, 100	810.70	849.04	57R-6, 30	813.00	851.34	Slump
57R-6, 30	813.00	851.04	57R-6, 96	813.66	852.00	Turbidite
63R-2, 32	864.92	903.26	63R-2, 40	865.00	903.34	Turbidite
64R-4, 5	877.35	915.69	64R-4, 15	877.45	915.79	Turbidite
64R-5, 118	879.98	918.32	64R-5, 130	880.10	918.44	Turbidite
65R-1, 4	882.54	920.88	65R-1, 38	882.88	921.22	Turbidite
65R-2, 55	884.55	922.89	65R-2, 59	884.59	922.93	Turbidite
67R-6, 27	909.17	947.51	67R-CC, 25	911.33	949.67	Turbidite
69R-1, 145	922.15	960.49	69R-2, 38	922.58	960.92	Turbidite
69R-4, 40	925.60	963.94	69R-4, 54	925.74	964.08	Turbidite
69R-6, 27	928.47	966.81	69R-6, 37	928.57	966.91	Turbidite
69R-CC, 0	929.69	968.03	69R-CC, 6	929.75	968.09	Turbidite
154-925B-						
30H-2, 55	272.55	305.39	30H-3, 40	273.90	306.74	Slump
154-925C-						
23H-6, 55	214.05	242.16	23H-6, 145	216.45	243.06	Slump
154-925D-						
23H-2, 120	214.20	237.98	23H-4, 90	216.90	240.68	Slump
29H-6, 30	276.30	305.19	30H-1, 30	278.30	309.20	Slump
154-926A-						
20H-5, 60	181.60	203.58	20H-5, 90	181.90	203.88	Turbidite
21H-1, 40	184.90	207.59	21H-1, 45	184.95	207.64	Turbidite
24H-5, 10	219.10	243.70	24H-5, 24	219.24	243.84	Turbidite
154-926B-						
15H-4, 5	135.05	151.92	15H-4, 15	135.15	152.02	Turbidite
16H-2, 58	142.08	160.42	16H-2, 61	142.11	160.45	Turbidite
20H-2, 140	180.90	203.59	20H-3, 17	181.17	203.86	Turbidite
24H-2, 70	221.20	246.72	24H-2, 78	221.28	246.80	Turbidite
154-926C-						
15H-7, 32	142.82	160.27	15H-CC, 5	142.85	160.30	Turbidite
20H-3, 38	184.38	203.80	20H-3, 68	184.68	204.10	Turbidite
24H-4, 135	224.85	243.76	24H-4, 140	224.90	243.81	Turbidite
154-927A-						
23H-2, 50	211.00	231.12	23H-3, 35	212.35	232.47	Slump
25H-1, 50	227.50	248.75	25H-2, 80	229.00	250.55	Slump
25H-7, 10	236.10	257.35	27H-1, 105	247.05	269.19	Slump
28H-3, 45	258.95	283.35	28H-3, 60	259.10	283.50	Turbidite
164-927B-						
22H-5, 100	202.00	222.45	22H-5, 120	202.20	222.65	Turbidite
22H-5, 125	202.25	222.70	22H-5, 130	202.30	222.75	Turbidite
23H-3, 110	208.60	232.72	23H-7, 27	213.77	237.89	Slump
25H-4, 140	229.40	255.12	25H-4, 150	229.50	255.22	Turbidite
25H-5, 0	229.50	255.22	25H-5, 95	230.45	256.17	Turbidite
26H-1, 95	233.95	259.31	26H-7, 3	242.03	267.39	Slump
154-927C-						
23H-2, 132	211.82	236.41	23H-3, 50	212.50	237.09	Slump
24H-5, 30	224.80	250.44	24H-5, 40	224.90	250.54	? Slump
25H-1, 17	228.17	256.34	25H-3, 140	232.40	256.57	Slump
25H-3, 92	231.92	260.09	25H-3, 96	231.96	260.13	Turbidite
154-928A-						
15H-5, 100	139.00	152.00	15H-5, 117	139.17	152.17	Turbidite
18H-1, 0	160.50	178.01	19H-4, 85	161.35	178.86	Slump
20H-1, 24	179.74	198.26	20H-1, 27	179.77	198.29	Turbidite
20H-1, 83	180.33	198.85	20H-1, 87	180.37	198.89	Turbidite
20H-1, 133	180.83	199.35	20H-1, 136	180.86	199.38	Turbidite
20H-3, 140	183.90	202.42	20H-6, 85	183.35	201.87	Slump
21H-3, 0	192.00	211.05	21H-4, 65	194.15	213.20	Slump
23X-6, 50	216.00	235.05	24X-4, 60	222.80	235.65	Slump
25X-3, 40	230.80	249.85	25X-3, 150	231.90	250.95	Slump
26X-4, 0	241.60	260.65	26X-CC, 35	244.38	263.43	Slump
154-928B-						
18X-1, 91	157.11	175.86	18X-2, 6	157.18	175.93	Turbidite
18X-4, 20	160.32	179.07	19X-7, 65	175.55	194.40	Multiple slumps
18X-6, 57	163.69	182.44	18x-6, 63	163.75	182.50	Turbidite in slump
19X-4, 130	171.70	184.55	19X-4, 140	171.80	190.65	Turbidite in slump
20X-2, 65	177.65	196.56	20X-3, 25	178.75	197.66	Slump
20X-3, 120	179.70	198.61	21X-3, 56	188.76	208.50	Multiple slumps
24X-2, 80	216.50	236.24	24X-6, 55	222.25	241.99	Slump
25X-4, 55	228.95	248.69	25X-4, 113	229.53	249.27	Slump
25X-6, 90	232.30	252.04	25X-6, 105	232.45	252.19	Turbidite
26X-1, 80	234.40	254.14	26X-1, 95	234.45	254.29	Turbidite
28X-3, 80	256.70	276.44	28X-3, 95	256.85	276.59	Turbidite

Table 2 (continued).

Top			Base			
Core, section, interval (cm)	Depth (mbsf)	Depth (mcd)	Core, section, interval (cm)	Depth (mbsf)	Depth (mcd)	Notes
41X-3, 100	380.84	400.58	41X-3, 130	381.14	400.88	Turbidite
48X-6, 4	452.54	472.28	48X-6, 140	453.90	473.64	Slump
49X-2, 5	456.15	475.89	49X-6, 13	462.23	481.97	Slump
50X-5, 3	470.23	489.97	51X-2, 82	476.22	495.96	Slump
52X-1, 90	484.50	504.24	53X-2, 90	486.00	505.74	Slump
55X-3, 115	516.75	536.49	55X-6, 10	520.20	539.94	? Slump
56X-3, 0	525.20	544.94	56X-6, 70	530.40	550.14	? Slump
154-928C-						
18X-5, 55	159.05	176.11	18X-5, 65	158.15	176.21	Turbidite
18X-7, 15	161.65	178.71	20X-1, 97	172.87	192.53	Turbidite
19X-5, 140	169.60	190.32	19X-5, 150	169.70	190.42	Turbidite in slump
20X-4, 20	176.60	196.26	20X-4, 50	177.00	196.56	Turbidite
20X-4, 50	176.90	196.56	20X-CC, 20	181.48	201.14	Slump
20X-5, 30	178.20	197.86	20X-5, 35	178.25	197.91	Turbidite in slump
154-929A-						
1H-2, 65	2.15	2.15	1H-2, 68	2.18	2.18	Turbidite (silt/clay)
1H-2, 80	2.30	2.30	1H-2, 84	2.34	2.34	Turbidite (silt/clay)
2H-6, 90	12.90	13.95	2H-6, 93	12.93	13.98	Turbidite (silt/clay)
2H-6, 109	13.09	14.14	2H-6, 11	13.11	14.16	Turbidite (silt/clay)
3H-5, 106	21.06	22.68	3H-5, 114	21.14	22.76	Turbidite (silt/clay)
3H-6, 100	22.50	24.12	3H-6, 107	22.57	24.19	Turbidite (silt/clay)
4H-2, 33	25.33	27.42	4H-2, 34	25.34	27.43	Turbidite (silt/clay)
4H-4, 114	29.14	31.23	4H-4, 136	29.36	31.45	Turbidite (silt/clay)
5H-6, 82	41.32	44.42	5H-6, 9	41.49	44.59	Turbidite (silt/clay)
13H-6, 0	116.50	128.35	14H-1, 130	119.80	131.96	Thin turbidites
15H-4, 10	132.60	144.03	16H-4, 30	142.30	154.05	?slumped thin turbidites
17X-3, 9	150.19	163.45	17X-3, 10	150.20	163.46	Turbidite
17X-4, 7	151.67	164.93	17X-4, 8	151.68	164.94	Turbidite
17X-4, 46	152.06	165.32	17X-4, 47	152.07	165.33	Turbidite
18X-2, 90	159.20	171.99	18X-5, 132	164.12	176.91	Slump
20X-1, 0	176.10	190.65	21X-5, 147	193.17	207.72	Slump
20X-4, 117	181.77	196.32	20X-4, 121	181.81	196.36	Turbidite in slump
20X-4, 132	181.92	196.47	20X-4, 137	181.96	196.51	Turbidite in slump
20X-5, 33	182.43	196.98	20X-5, 36	182.46	197.01	Turbidite in slump
20X-6, 47	184.07	198.62	20X-6, 50	184.10	198.65	Turbidite in slump
20X-6, 56	184.16	198.71	20X-6, 58	184.18	198.73	Turbidite in slump
20X-7, 47	185.57	200.12	20X-7, 50	185.60	200.15	Turbidite in slump
22X-1, 135	196.75	210.99	22X-1, 140	196.80	211.04	Turbidite
22X-1, 140	196.80	211.04	22X-4, 147	201.37	215.61	Slump
22X-3, 63	199.03	213.27	22X-3, 65	199.05	213.29	Turbidite in slump
22X-3, 80	199.20	213.44	22X-3, 84	199.24	213.48	Turbidite in slump
22X-4, 3	199.93	214.17	22X-4, 6	199.96	214.20	Turbidite in slump
25X-2, 122	226.72	242.14	25X-2, 150	227.00	242.42	Turbidite
25X-5, 145	231.45	246.87	25X-6, 145	232.95	248.37	Thick turbidite
26X-3, 78	237.38	252.80	26X-4, 4	238.14	253.56	Thick turbidite
26X-6, 64	241.74	257.16	26X-6, 73	241.83	257.25	Turbidite
27X-2, 20	245.10	260.52	27X-2, 30	245.20	260.62	Turbidite
27X-3, 50	243.90	262.32	27X-4, 20	248.10	263.52	Thick turbidite
28X-3, 2	256.02	271.44	28X-3, 8	256.08	271.50	Turbidite
28X-4, 17	257.67	273.09	28X-4, 20	257.70	273.12	Turbidite
35X-3, 95	324.35	339.77	35X-3, 102	324.42	339.84	Turbidite
37X-6, 90	328.80	344.22	37X-6, 110	329.00	344.42	Thin slump
38X-5, 35	355.75	371.17	38X-5, 43	355.83	371.25	Turbidite
41X-4, 95	383.55	398.97	41X-4, 104	383.64	399.56	Turbidite
44X-2, 110	409.70	425.12	44X-5, 110	414.20	429.62	? Slump
45X-3, 85	420.55	435.97	46X-1, 130	427.70	443.12	Thin turbidites/slump
50X-5, 23	471.23	486.65	50X-5, 28	471.28	486.70	Turbidite
50X-6, 17	472.67	488.09	50X-6, 49	472.99	488.41	Turbidite
51X-5, 130	481.90	498.27	51X-6, 8	482.18	498.55	Turbidite
52X-6, 55	492.25	508.96	52X-6, 80	492.50	509.21	Turbidite
52X-6, 90	492.60	509.31	52X-CC, 29	493.07	509.78	Turbidite
53X-1, 107	494.57	510.91	53X-1, 124	494.74	511.08	Turbidite
154-929B-						
1H-2, 55	2.05	2.10	1H-2, 56	2.06	2.11	Turbidite (silt/clay)
1H-2, 73	2.23	2.28	1H-2, 76	2.26	2.31	Turbidite (silt/clay)
1H-3, 140	4.40	4.45	1H-3, 143	4.43	4.48	Turbidite (silt/clay)
2H-2, 112	12.12	12.74	2H-2, 113	12.13	12.75	Turbidite (silt/clay)
2H-5, 5	15.55	16.17	2H-5, 7	15.57	16.19	Turbidite (silt/clay)
3H-2, 106	21.56	22.69	3H-2, 107	21.57	22.70	Turbidite (silt/clay)
3H-3, 96	22.96	24.09	3H-3, 97	22.97	24.10	Turbidite (silt/clay)
3H-4, 138	24.88	26.01	3H-4, 139	24.89	26.02	Turbidite (silt/clay)
3H-5, 82	25.82	26.95	3H-5, 88	25.88	27.01	Turbidite (silt/clay)
3H-5, 108	26.08	27.21	3H-5, 110	26.10	27.23	Turbidite (silt/clay)
3H-5, 121	26.21	27.34	3H-5, 122	26.22	27.35	Turbidite (silt/clay)
4H-1, 80	29.30	31.90	4H-1, 83	29.33	31.93	Turbidite (silt/clay)
4H-4, 112	34.12	36.72	4H-4, 114	34.14	36.74	Turbidite (silt/clay)
5H-3, 54	41.54	44.62	5H-3, 57	41.57	44.65	Turbidite (silt/clay)
13H-5, 0	120.00	128.31	14X-1, 117	124.67	133.48	Thin turbidites (? slumped)
15X-2, 10	134.70	143.19	15X-2, 130	135.90	144.39	? Slump
17X-3, 137	156.57	164.96	18X-4, 106	167.36	177.67	Slump (top and base uncertain)
18X-4, 106	167.36	177.67	18X-4, 110	167.40	177.71	Turbidite
19X-6, 85	179.75	190.90	19X-6, 95	179.85	191.00	Turbidite

Table 2 (continued).

Top			Base			
Core, section, interval (cm)	Depth (mbsf)	Depth (mcd)	Core, section, interval (cm)	Depth (mbsf)	Depth (mcd)	Notes
19X-7, 40	180.80	192.50	19X-CC, 1	180.80	191.95	Turbidite
20X-1, 100	182.00	191.85	22X-3, 86	204.26	215.70	Slump
20X-2, 33	182.83	192.68	20X-2, 37	182.87	192.72	Turbidite in slump
20X-2, 41	182.91	192.76	20X-2, 45	182.95	192.80	Turbidite in slump
20X-4, 104	186.54	196.39	20X-4, 110	186.60	196.45	Turbidite in slump
21X-4, 86	196.06	206.58	21X-4, 88	196.08	206.60	Turbidite in slump
21X-6, 32	198.52	209.04	21X-6, 100	199.20	209.72	Turbidite in slump
22X-1, 147	201.87	213.31	22X-2, 2	201.92	213.36	Turbidite in slump
22X-2, 13	202.03	213.47	22X-2, 25	202.15	213.59	Turbidite in slump
22X-2, 87	202.77	214.21	22X-2, 93	202.83	214.27	Turbidite in slump
154-929C-						
1H-2, 20	3.86	4.62	1H-2, 21	3.87	4.63	Turbidite (silt/clay)
2H-7, 35	21.85	22.68	2H-CC, 1	21.89	22.72	Turbidite (silt/clay)
3H-2, 86	24.36	25.78	3H-2, 87	24.37	25.79	Turbidite (silt/clay)
3H-2, 110	24.60	26.02	3H-2, 111	24.61	26.03	Turbidite (silt/clay)
3H-3, 53	25.53	26.95	3H-3, 54	25.54	26.96	Turbidite (silt/clay)
3H-3, 60	25.60	27.02	3H-3, 61	25.61	27.03	Turbidite (silt/clay)
3H-3, 65	25.65	27.07	3H-3, 66	25.66	27.08	Turbidite (silt/clay)
3H-3, 87	25.87	27.29	3H-3, 88	25.88	27.30	Turbidite (silt/clay)
3H-3, 99	25.99	27.41	3H-3, 100	26.00	27.42	Turbidite (silt/clay)
3H-6, 81	30.31	31.73	3H-6, 83	30.33	31.75	Turbidite (silt/clay)
13H-2, 130	119.80	128.30	13H-6, 30	124.80	133.30	Thin turbidites
15H-3, 103	140.13	148.84	15X-4, 15	140.75	149.46	Turbidite
15X-4, 62	141.22	149.93	15X-5, 25	142.35	151.06	? Thin turbidites
154-929D-						
1H-2, 35	1.85	2.26	1H-2, 36	1.86	2.27	Turbidite (silt/clay)
1H-2, 50	2.00	2.41	1H-2, 54	2.04	2.45	Turbidite (silt/clay)
1H-3, 105	4.05	4.46	1H-3, 106	4.06	4.47	Turbidite (silt/clay)
2H-4, 142	12.92	13.58	2H-4, 143	12.93	13.59	Turbidite (silt/clay)
2H-5, 11	13.11	13.77	2H-5, 12	13.12	13.78	Turbidite (silt/clay)
2H-6, 74	15.24	15.90	2H-6, 75	15.25	15.91	Turbidite (silt/clay)
3H-5, 124	23.74	25.67	3H-5, 125	23.75	25.68	Turbidite (silt/clay)
3H-6, 108	25.08	27.01	3H-6, 110	25.10	27.03	Turbidite (silt/clay)
3H-6, 111	25.11	27.04	3H-6, 112	25.12	27.05	Turbidite (silt/clay)
3H-6, 113	25.13	27.06	3H-6, 115	25.15	27.08	Turbidite (silt/clay)
4H-4, 49	30.99	33.25	4H-4, 51	31.01	33.27	Turbidite (silt/clay)
5H-4, 147	41.47	44.69	5H-4, 148	41.48	44.70	Turbidite (silt/clay)
154-929E-						
1R-2, 10	472.21	487.92	1R-2, 60	472.71	488.42	Turbidite
2R-1, 100	482.24	498.24	2R-1, 123	482.53	498.47	Turbidite
3R-3, 60	494.60	509.37	3R-3, 100	495.00	509.77	Turbidite
5R-2, 30	512.20	524.00	5R-2, 60	512.50	524.30	? Slump
6R-1, 0	520.00	531.80	6R-1, 125	521.25	533.05	Slump
8R-CC, 0	544.37	556.17	8R-CC, 10	544.47	556.27	Turbidite
9R-1, 0	548.60	560.40	9R-1, 117	549.77	561.57	Slump
10R-6, 50	566.30	578.10	10R-6, 75	566.55	578.35	Turbidite
11R-2, 60	570.00	581.80	11R-4, 60	573.00	584.80	Slump
13R-1, 109	588.29	600.09	13R-1, 118	588.38	600.18	Turbidite
13R-2, 48	589.18	600.98	13R-2, 54	589.24	601.04	Turbidite
13R-2, 141	590.11	601.91	13R-2, 144	590.14	601.94	Turbidite
13R-5, 80	594.00	605.80	13R-5, 85	594.05	605.85	Turbidite
14R-3, 45	600.35	612.15	14R-3, 54	600.44	612.24	Turbidite
15R-2, 111	609.11	620.91	15R-2, 115	609.15	620.94	Turbidite
15R-2, 115	609.15	620.95	15R-5, 13	612.63	624.43	Slump
15R-6, 30	614.30	626.10	15R-6, 42	614.42	626.22	Turbidite
16R-2, 10	617.70	629.50	16R-2, 135	618.95	630.75	Slump

Note: Turbidite = Calcareous turbidite or grain flow unless otherwise indicated; Slump = Slump or slide.

HIGH-RESOLUTION CARBONATE AND TERRIGENOUS FLUX RECONSTRUCTIONS

Having established relationships that enable us to use the high-resolution MST and color data to extend the measured percentage carbonate data (sampled at several 1 meter intervals), and having developed high-resolution time series for the five sites, we are in a position to examine the history of the terrigenous flux, the biogenic carbonate flux, and the carbonate dissolution fluxes over the transect. Here we demonstrate the power of the data set by examining the record for the last 7 m.y. Based on the patterns in Figure 3, we concluded that the natural gamma data provide the most robust estimate of percentage of carbonate, and proceeded to calculate percentage of carbonate, averaged in 0.1-m.y. increments, for each site (Fig. 9). Among the shallow sites there is a small, systematic difference between the data for the southerly sites (925 and 926) and Site 927, which is closer to the Amazon and has a slightly lower carbonate content. Among these sites, the most important feature of Figure 9 is the decreasing percentage of carbonate over the past 7 m.y. That this reflects an increase in the dilution by noncarbonate is confirmed by the lower panel, which shows the changing terrigenous mass accumulation at Site 927 over the past 7 m.y. The percentage carbonate data from the deeper sites tells a different story: The CCD was evidently close to the depth of Site 928 and above Site 929 at 7 Ma and moved deeper, so that by 4.5 Ma Site 928 was above the lysocline and had the same carbonate content as Site 926. Site 929 emerged from red clay deposition after 5.7 Ma. Older than 5.7 Ma, the sediments at Site 929 are dominated by red clays but are interbedded with both in-place and allochthonous material with higher carbonate content. Superimposed on the long-term decrease in carbonate percentage caused by increasing terrigenous input is a narrowing of the difference in carbonate between the shallow and deep sites, which implies improved carbonate preservation (a deepening lysocline) since that time. Evidently, the modern bathymetric gradient of carbonate preservation became established at about 4.5 Ma.

Table 3. Tie-points based on graphic correlation of composite magnetic susceptibility records of Sites 925 through 929.

Events	Site 926 (mcd)	Age (Ma)	Site 925 (mcd)	Site 927 (mcd)	Site 928 (mcd)	Site 929 (mcd)
Tie	0.01	0	0.03	0.05	0.04	0.05
Tie	4.84	0.138	4.93	6.05	5.04	6.10
Tie	9.44	0.269	9.48	11.90	10.02	11.11
Tie	12.88	0.367	13.05	16.06	13.44	14.83
Tie	18.10	0.526	19.85	22.75	18.88	20.02
Tie	24.06	0.726	26.24	30.76	25.91	27.86
Tie	29.03	0.893	30.92	37.15	31.05	33.06
Tie	34.84	1.088	36.88	44.24	36.55	38.96
Tie	39.11	1.231	41.78	49.73	41.55	44.02
Add. Tie 927	41.36	1.307		52.75		
Tie	42.61	1.349	45.34	54.05	45.03	47.52
Tie	46.16	1.468	48.71	56.75	48.51	51.11
Tie	49.21	1.570	51.32	59.75	51.46	54.04
Tie	54.78	1.757	56.57	64.95	56.68	59.40
Tie	60.30	1.942	62.21	71.12	62.57	65.15
Tie	62.97	2.027	65.03	78.12	65.25	67.78
Add. Tie 927	66.56	2.140		82.73		71.31
Tie	68.96	2.215	71.49	85.97	71.58	73.67
Tie	73.28	2.351	75.94	91.17	76.17	77.96
Tie	79.34	2.542	81.60	97.57	82.51	84.02
Tie	86.64	2.772	88.09	104.38	89.02	90.33
Tie	90.83	2.904	92.82	109.23	93.64	93.57
Tie	93.46	2.986	95.51	111.84	96.44	95.91
Slump 925	95.15	3.040	97.24			
Slump 925	95.16	3.040	99.55			
Tie	96.35	3.077	100.39	114.78	99.34	98.52
Tie	101.12	3.227	106.03	120.08	104.64	103.32
Tie	104.49	3.333	109.02	123.70	108.45	106.17
Tie	108.14	3.448	113.04	128.35	112.70	109.46
Tie	114.50	3.649	118.73	134.59	118.17	114.15
Tie	119.93	3.828	124.27	139.75	122.92	117.75
Tie	122.99	3.942	127.21	142.95	125.36	120.01
Add. Tie 929	125.54	4.037				122.21
Tie	129.44	4.182	133.09	148.8	130.26	124.60
Tie	134.00	4.351	137.05	152.94	133.68	127.35
Tie	136.57	4.446	139.62	155.39	135.14	128.85
Tie	142.30	4.659	144.41	161.46	139.55	132.93
Tie	145.68	4.785	148.00	165.23	142.61	135.37
Tie	149.97	4.944	152.33	169.71	146.73	138.13
Tie	153.77	5.085	156.26	173.41	150.09	140.17
Tie	158.50	5.261	160.91	178.47	153.59	143.78
Tie	162.91	5.425	165.43	183.07	156.66	146.88
Tie	166.07	5.542	168.92	186.48	159.41	148.86
Tie	171.10	5.729	174.12	190.78	162.85	151.7
Tie	175.72	5.913	178.54	194.87	165.91	
Slump 925	177.48	6.017	180.72			
Slump 925	177.53	6.020	182.07			
Tie	179.13	6.115	184.21	198.78	167.92	
Tie	180.88	6.218	187.21	200.49	168.93	
Tie	183.16	6.353	191.67	202.99	171.34	
Slump 925	186.49	6.550	195.72			
Slump 925	186.81	6.569	204.33			
Tie	188.61	6.676	206.39	209.02	174.54	
End 928	192.99	6.935			178.07	
Tie	194.05	6.998	212.60	215.16		
Tie	197.61	7.209	218.51	218.65		
Tie	203.82	7.577	225.65	225.22		
Tie	208.59	7.859	233.05	229.99		
Tie	214.14	8.188	238.51	234.32		
Slump 925	216.64	8.336	241.01			
Slump 925	216.69	8.339	242.03			
Tie	220.12	8.517	246.23	240.79		
Tie	224.10	8.711	250.49	244.41		
Add. Tie 927	228.31	8.917		247.37		
Tie	234.22	9.205	271.27	253.37		
Tie	238.39	9.415	277.33	257.60		
Tie	243.84	9.859	283.08	265.51		
Tie	249.90	10.353	293.01	271.18		
Slump 927	250.07	10.367		278.79		
Tie	251.65	10.496	295.64	280.63		
Tie	254.34	10.716	298.94	283.50		
Tie	256.61	10.901	301.39	285.55		
Tie	259.67	11.150	305.79	287.95		
Tie	261.11	11.268	308.11	289.14		
Tie	263.86	11.492	311.89	291.49		
Tie	268.11	11.816	316.14	295.45		
Tie	270.39	11.971	318.35	298.21		
Tie	273.13	12.158	321.50	302.76		
Tie	277.76	12.473	328.13	307.41		

Notes: Additional tie-points that were used only for a single site are marked in the "Events" column. The ages for the tie-points were obtained from selected nannofossil events for Site 926 (see Table 3, "Site 926" chapter, this volume).

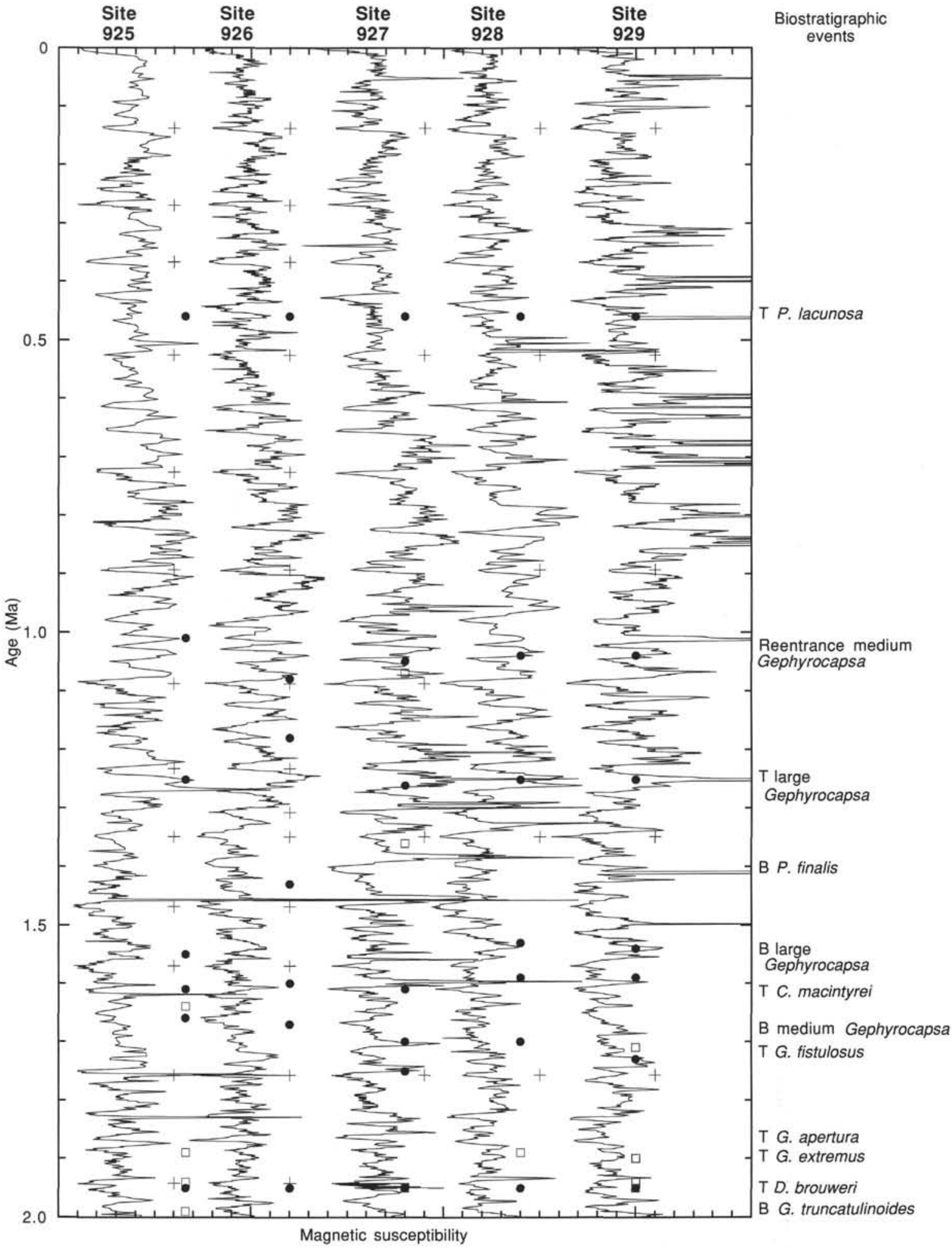

Figure 8. Composite magnetic susceptibility records of Sites 925 through 929 vs. age for the last 6 m.y. Sites 925, 927, 928, and 929 were correlated to Site 926 based on the graphic correlation tie-points listed in Table 3. The ages for the tie-points were obtained from selected nannofossil events of Site 926 (see table 3, "Site 926" chapter, this volume) and transferred to the other sites by means of this correlation. Biostratigraphic events are shown on the interpolated ages based on this correlation. Tie-points = plus signs, nannofossil datums = closed circles, and foraminifers = open squares. T = top occurrence, B = bottom occurrence, and S to D = sinistral to dextral coiling.

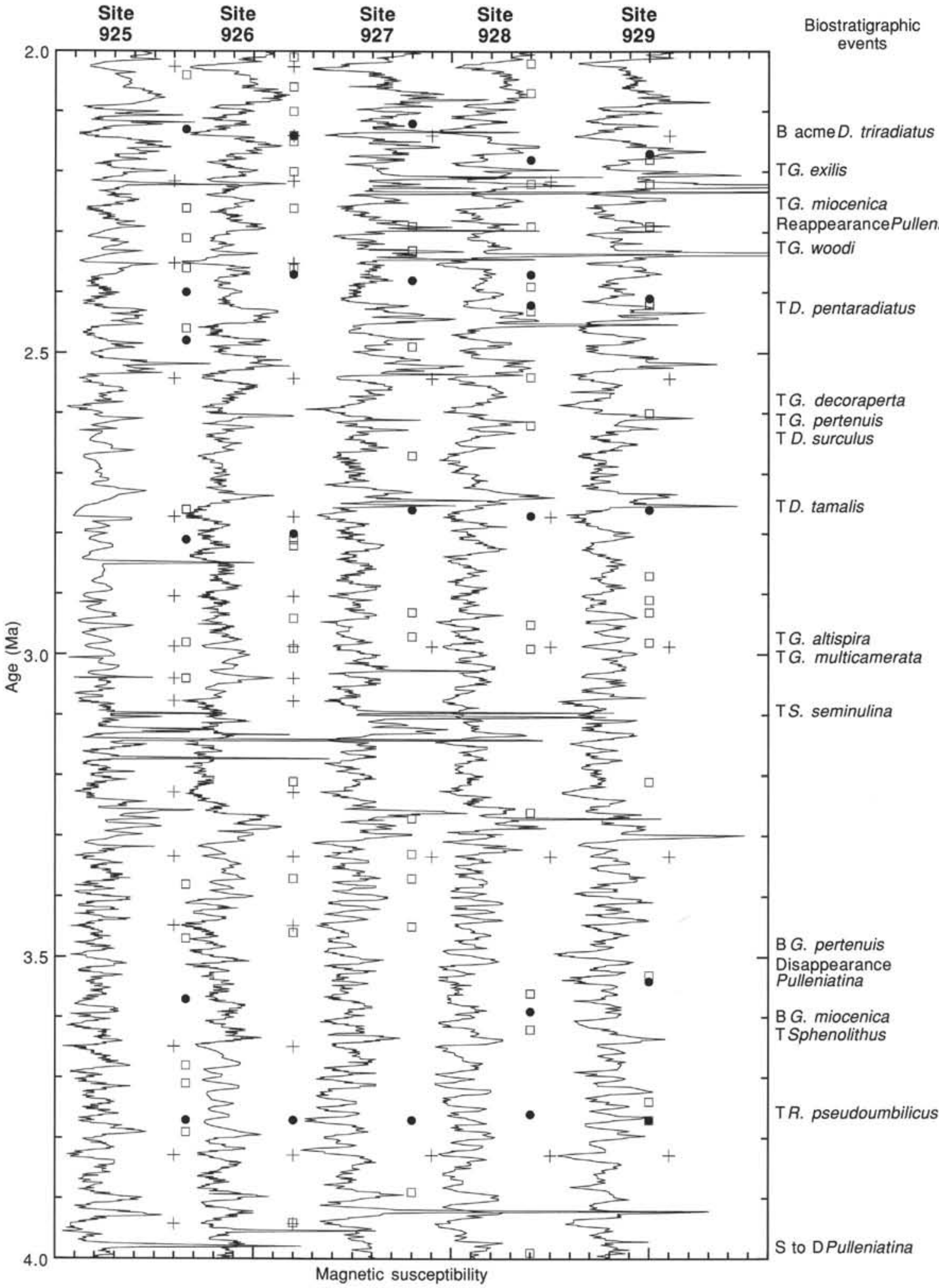

Figure 8 (continued).

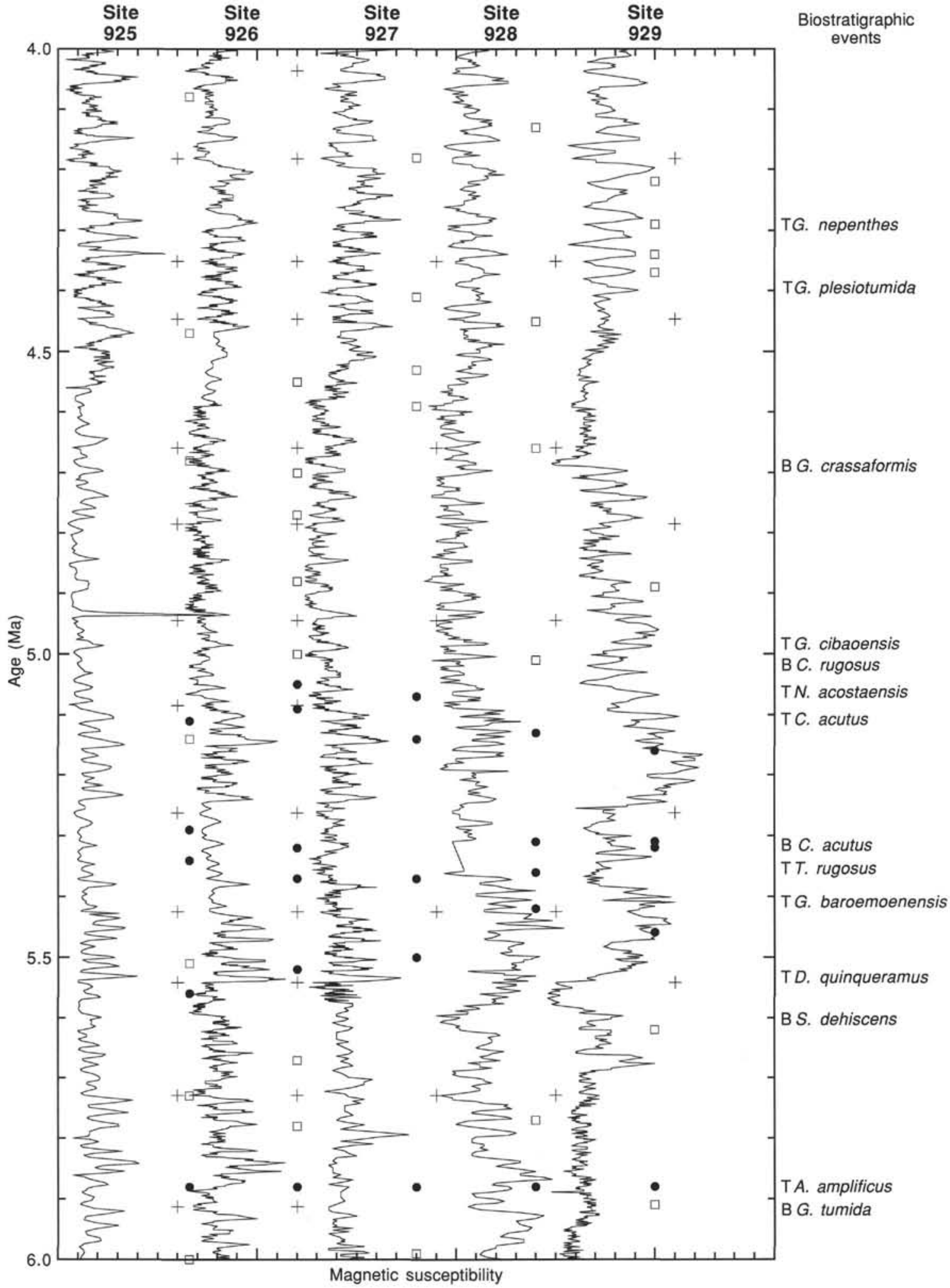

Figure 8 (continued).

Table 4. Age estimates of biostratigraphic datums in each site determined after high-resolution correlation between Leg 154 sites.

			Site 925		Site 926		Site 927		Site 928		Site 929	
	Marker species	Literature age (Ma)	Depth (mcd)	Age (Ma)	Depth (mcd)	Age (Ma)	Depth (mcd)	Age (Ma)	Depth (mcd)	Age (Ma)	Depth (mcd)	Age (Ma)
T	*P. lacunosa*	0.46	18.40	0.46	16.14	0.46	21.17	0.46	16.78	0.46	18.67	0.46
Reentrance medium	*Gephyrocapsa*	1.03	34.45	1.01	34.61	1.08	42.81	1.05	35.18	1.04	37.65	1.04
T large	*Gephyrocapsa*	1.24	42.09	1.25	37.76	1.18	51.14	1.26	42.11	1.25	44.60	1.25
B	*P. finalis*	1.40	65.40	2.04	63.99	2.06	82.17	2.12	66.67	2.07	65.42	1.95
B large	*Gephyrocapsa*	1.46	50.91	1.55	45.18	1.43	61.05	1.61	50.34	1.53	53.10	1.54
T	*C. macintyrei*	1.60	52.41	1.61	50.07	1.60	63.34	1.70	52.02	1.59	54.54	1.59
B medium	*Gephyrocapsa*	1.67	53.91	1.66	52.12	1.67	64.85	1.75	55.00	1.70	58.26	1.73
T	*G. fistulosus*	1.70	60.77	1.89	62.50	2.01	75.38	1.95	65.18	2.02	72.42	2.18
T	*G. apertura*	1.90	53.47	1.64	66.79	2.15	43.67	1.07	61.00	1.89		
T	*G. extremus*	1.90	63.78	1.99	65.49	2.10	54.41	1.36	78.72	2.43	57.69	1.71
T	*D. brouweri*	1.95	62.44	1.95	60.53	1.95	76.02	1.95	62.29	1.95	65.41	1.95
B	*G. truncatulinoides*	1.90	62.27	1.94	66.79	2.14	75.38	1.95	71.80	2.22	63.92	1.90
B acme	*D. triradiatus*	2.15	68.64	2.13	66.73	2.14	82.11	2.12	69.59	2.18	72.16	2.17
T	*G. exilis*	2.20	73.02	2.26	68.56	2.20	88.95	2.29	74.01	2.29		
T	*G. miocenica*	2.30	76.07	2.36	73.56	2.36	90.44	2.33	77.60	2.39	80.23	2.42
Reappearance	*Pulleniatina*	2.30	74.46	2.31	70.53	2.26	88.95	2.29	74.01	2.29	76.17	2.29
T	*G. woodi*	2.30	74.46	2.31								
T	*D. pentaradiatus*	2.44	77.36	2.40	73.86	2.37	92.04	2.38	76.94	2.37	79.74	2.41
T	*G. decoraperta*	2.60	87.70	2.76	88.24	2.82	95.99	2.49	82.44	2.54	92.93	2.87
T	*G. pertenuis*	2.60	79.24	2.46	84.50	2.81	101.82	2.67	84.67	2.62		
T	*D. surculus*	2.61	79.86	2.48					78.53	2.42		
T	*D. tamalis*	2.76	89.31	2.81	87.72	2.80	104.74	2.76	88.89	2.77	90.02	2.76
T	*G. altispira*	3.00	97.87	3.04	93.47	2.99	111.98	2.97	96.66	2.99	95.93	2.98
T	*G. multicamerata*	3.00	95.17	2.98	91.97	2.94	110.64	2.93	95.17	2.95	94.43	2.93
T	*S. seminulina*	3.10	97.90	3.04	101.24	3.21	111.98	2.97	106.37	3.26	103.03	3.21
B	*G. pertenuis*	3.50	114.00	3.47	109.01	3.46	128.80	3.45	117.85	3.62		
Disappearance	*Pulleniatina*	3.50	111.03	3.38	106.01	3.37	124.26	3.33	116.36	3.56	111.88	3.53
B	*G. miocenica*	3.60	120.52	3.68	106.01	3.37	125.80	3.37	126.68	3.99	117.11	3.77
T	*Sphenolithus*	3.62	117.18	3.57			121.49	3.27	117.18	3.59	112.14	3.54
T	*P. pseudoumbilicus*	3.77	122.88	3.77	118.36	3.77	138.45	3.77	121.37	3.76	116.61	3.77
S to D	*Pulleniatina*	4.00	131.04	4.08	123.59	3.94						
T	*G. nepenthes*	4.30	140.68	4.47	139.77	4.55	154.93	4.41	135.87	4.45	128.18	4.37
T	*G. plesiotumida*	4.40	121.45	3.71	145.77	4.77	142.00	3.89	129.68	4.13	125.64	4.22
B	*G. crassaformis*	4.70	123.96	3.79								
T	*G. cibaoensis*	5.00	158.23	5.14	145.77	4.77	159.88	4.59				
B	*C. rugosus*	5.04	157.60	5.11	153.44	5.05	173.59	5.07	151.64	5.13	142.21	5.16
T	*N. acostaensis*	5.10	145.72	4.68	143.77	4.70	149.21	4.18	140.12	4.66	126.86	4.29
T	*C. acutus*	5.04	157.60	5.11	154.52	5.09	175.57	5.14	151.64	5.13	142.21	5.16
B	*C. acutus*	5.34	163.35	5.34	161.96	5.37	182.03	5.37	155.11	5.31	145.18	5.31
T	*T. rugosus*	5.34	162.30	5.29	160.46	5.32			155.11	5.36	145.18	5.32
T	*G. baroemoenensis*	5.40	158.23	5.14	148.77	4.88						
T	*D, quinqueramus*	5.56	169.62	5.56	165.64	5.52	185.88	5.50	157.11	5.42	148.08	5.46
B	*S. dehiscens*	5.60	168.33	5.51	152.82	5.00	158.38	4.53	148.71	5.01	137.72	4.89
T	*A. amplificus*	5.88	179.40	5.88	175.17	5.88	194.67	5.88	166.09	5.88	150.80	5.88
B	*G. tumida*	5.90	174.79	5.73	169.94	5.67	204.88	6.41	164.09	5.77	150.71	5.62
B	*G. margaritae*	6.20	180.79	6.00	172.94	5.78	196.71	5.99			156.81	5.91

Notes: T = top occurrence, B = bottom occurrence, and S to D = sinistral to dextral coiling.

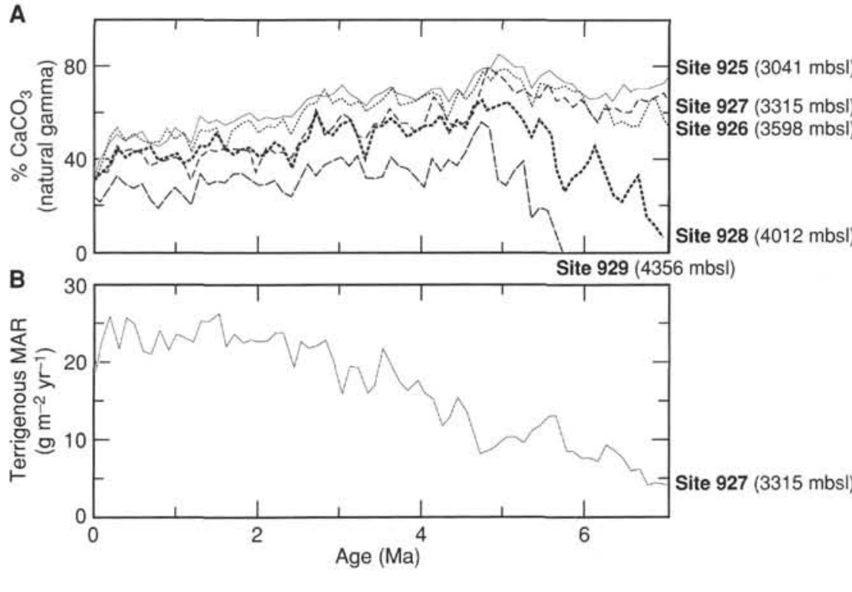

Figure 9. **A.** Record of carbonate concentration in Ceara Rise sediments 0 to 7 Ma. Carbonate concentration was estimated from the regression relationship between carbonate and natural gamma emission using data spanning the past 7 m.y. The relationships are developed for the northern (Sites 927, 928, and 929) and southern (Sites 925 and 926) sites separately. Large differences between carbonate concentrations in shallow and deep sites before 4.5 Ma document a late Miocene and very early Pliocene episode of severe dissolution. During this period, and for much of the Miocene, the deep waters were corrosive enough to have removed most of the carbonate from the sediments below a water depth of 4000 m. Severe dissolution during the Miocene contributed to the widespread occurrence of hiatuses reported over much of the Atlantic basin (Wright et al., 1992). **B.** Variations over the last 7 m.y. in the mass accumulation rate of terrigenous material at Site 927, the closest of the shallow sites to the Amazon Fan.

LOW-RESOLUTION CARBONATE AND TERRIGENOUS FLUX RECONSTRUCTIONS

The sediments recovered from the Ceara Rise sites are primarily a mixture of calcium carbonate and terrigenous material. The concentration of biogenic opal is only high enough to affect terrigenous flux estimates at Site 929, the deepest site drilled, within sediments of early Oligocene age. The organic carbon content is low at all sites, reflecting the pelagic nature of sediments on the Ceara Rise and its location away from areas of strong primary productivity and upwelling.

One of the primary objectives of Leg 154 was to obtain a depth transect of calcium carbonate deposition on the Ceara Rise that would provide a history of carbonate production and dissolution during the Cenozoic. Shipboard carbonate and density measurements, along with age models based on biostratigraphic datums, were used to quantify the mass accumulation rate (MAR) of calcium carbonate at the five sites drilled to provide a broad-scale view of carbonate production during the Cenozoic. Because the sediments are a mixture of carbonate and terrigenous material, the noncarbonate accumulation rate obtained from the difference between bulk sedimentation and carbonate accumulation provides a history of terrigenous accumulation at the Ceara Rise. Presently, these terrigenous sediments are derived from Amazon River outflow.

The history of calcium carbonate MAR for the Leg 154 sites may be described in terms of four distinct periods (Fig. 10). After an initial decrease in the earliest Eocene, the MAR remains low throughout the Eocene, with mean rate at the shallow Site 925 being twice that at the deep Site 929 within the interval common to both sites. A marked increase in MAR occurred during the Oligocene, with mean rate at Site 925 reaching near 60 g/m^2/yr and the preservation of calcareous microfossils being relatively good throughout this interval. The MAR dropped during the early and middle Miocene, with all sites exhibiting poor preservation of carbonate. Accumulation generally increased after 10 Ma, particularly at the shallow sites. This last interval contains a drop in carbonate MAR at all sites for the Pleistocene. This pattern of accumulation is highlighted in Figure 11, where the accumulation rates are presented relative to the rate at Site 925 (the shallowest site) for four time intervals spanning the past 30 Ma. The shallow-to-deep relative gradient in accumulation is greatest during the interval from 5.88 to 16.8 Ma, which suggests a shoaling of the carbonate compensation depth during this time. This same pattern of high carbonate accumulation during the Oligocene and low rates during the Miocene was observed in the Indian Ocean depth transect from the Mascarene Plateau (Peterson et al., 1992).

The MAR of noncarbonate material shows similar large variations through time, with relatively high rates throughout much of the Paleogene. The noncarbonate MAR is low from 20 to 10 Ma, with a dramatic increase at all sites after that time. This increase is greater at the northern sites (927, 928, and 929; Figs. 7 and 11). The large increase since the late Miocene may be mostly related to accelerated erosion of the Andes caused by accelerated uplift (Benjamin et al., 1987) and/or global cooling.

INTERSTITIAL WATERS

Interstitial-water geochemistry across the Ceara Rise depth transect is consistent with the biogenic-rich nature of the sediments; it is affected by low to moderate organic carbon input and burial at the sites. Dissolved silica and alkalinity profiles indicate some variability in biogenic sediment inputs to the sites through time, and site-to-site differences in silica suggest some variability in bottom-water chemistry. Dissolved lithium concentrations are unusually high at all the Ceara Rise sites, and no simple explanation for these values is known.

Sulfate reduction is incomplete at all five sites in the depth transect, with sulfate reduced from seawater concentrations by 55%–70% at the base of each cored interval (Fig. 12). This extent of sulfate reduction is significantly greater than typically found at pelagic carbonate sites (Leg 130, Kroenke, Berger, Janecek, et al., 1991; Leg 138, Mayer, Pisias, Janecek, et al., 1992) and indicates relatively low organic matter burial at the Ceara Rise. Site-to-site differences in sulfate reduction are minimal, with the exception that the pore waters at Site 929 have undergone significantly less sulfate reduction than those at the shallower sites. This suggests less organic carbon burial at Site 929, as a function of greater water depth and/or lower sedimentation rates at that site.

Dissolved silica profiles are similar at all sites, with maxima at each site in pore waters recovered from sediments of early Miocene age at each side (Fig. 13). At Site 929, the deepest site in the depth transect, there is an additional silica peak in the pore waters recovered from early Oligocene sediments. At Site 925, the only other site where interstitial water was recovered from early Oligocene sediments, silica concentrations are low in that interval. At all five sites, concentrations of pore-water silica and the opaline sediment component covaried downsection. The high pore-water silica concentrations indicate that the original concentration of buried opal was greater than is presently preserved. The intervals in which siliceous microfossils are found may indicate times of higher biogenic silica production in the surface waters, with higher sedimentation rates enhancing silica

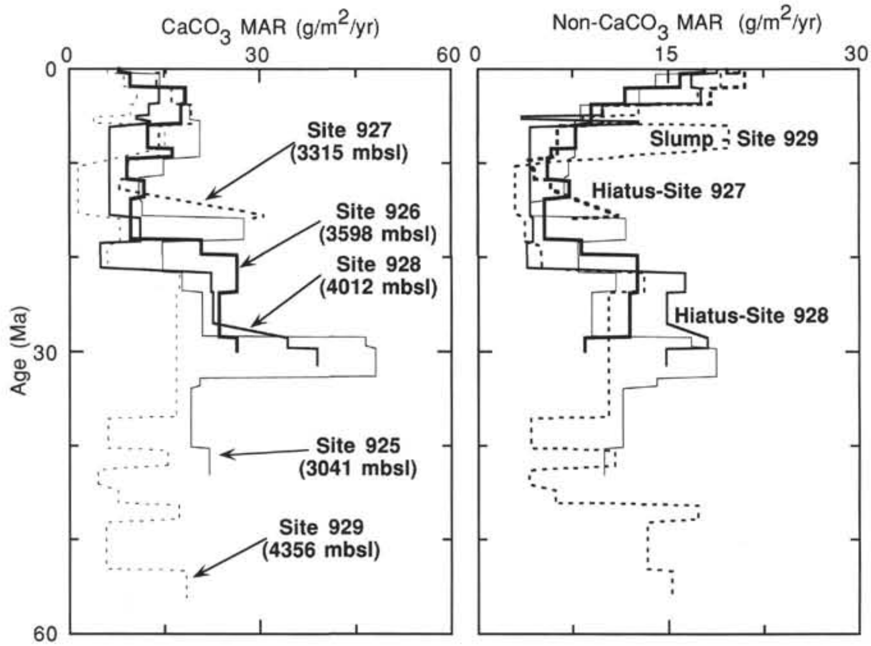

Figure 10. Mean calcium carbonate and noncarbonate mass accumulation rates (MARs) vs. age for Sites 925 through 929. Note that the scale for the carbonate is twice the range of the noncarbonate MAR in the separate plots.

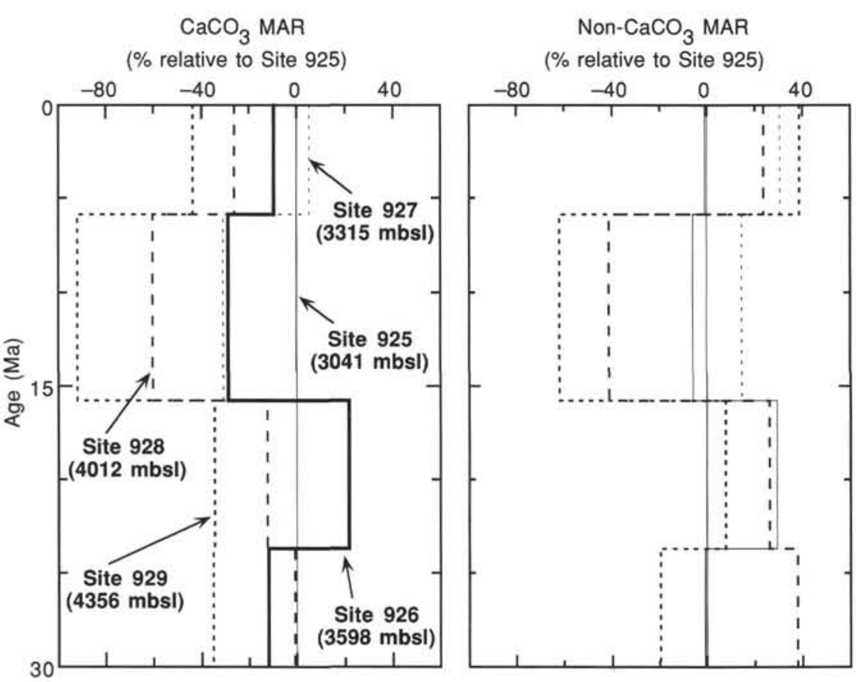

Figure 11. Mean calcium carbonate and noncarbonate mass accumulation rates (MARs) for Leg 154 sites during the time intervals 0–5.88, 5.88–16.8, 16.8–23.7, and 23.7–30 Ma, shown as the percentage difference from the rate at Site 925.

burial at the seafloor (see "Biosiliceous Sedimentation" section, this chapter). The alkalinity profiles (Fig. 13) support this explanation, as alkalinity and silica peaks co-occur at each site. The alkalinity maxima indicate that organic carbon burial and subsequent degradation and/or calcium carbonate dissolution were higher in these intervals, which would also have contributed to a faster burial rate of siliceous sediments. The accumulation of opal in the early Oligocene at Site 929 and not at Site 925 most likely indicates a difference in preservation, rather than a difference in surface-water inputs to the sites. In particular, deeper southern component water is relatively silica enriched, which would have enhanced the preservation of silica deposited on the seafloor at the deepest site (Site 929), in contrast to the silica-depleted northern component water that may have intercepted the seafloor at the shallower Site 925.

Lithium concentrations were extraordinarily high at all five sites (Fig. 13), with concentrations nearly 100 times greater than in pore water analyzed at other pelagic carbonate sites (Leg 130, Kroenke, Berger, Janecek, et al., 1991; Leg 138, Mayer, Pisias, Janecek, et al., 1992). Concentrations measured at the Ceara Rise are in the same range as those in pore waters from the Guaymas Basin, and from the Peru Margin. The high pore-water lithium in the Guaymas Basin samples was attributed to the effects of high-temperature basalt alteration (>200°C; Gieskes et al., 1982). High pore-water lithium in Peru continental slope sediments was attributed to exchange with underlying continental crust (ODP Sites 683 and 685) and oceanic crust (ODP Sites 682 and 688) at high temperatures (Martin et al., 1991). Although the dissolution of biogenic silica has been suggested as a source of lithium to the pore waters (Gieskes, 1981), the lithium and

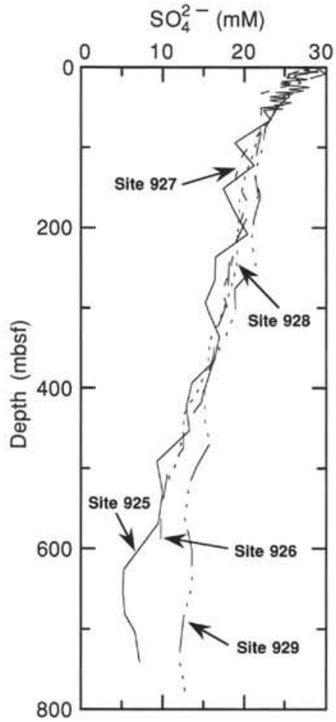

Figure 12. Sulfate in pore waters vs. depth at all sites.

silica profiles are actually quite different at all the Ceara Rise sites, and also at other pelagic sites (Leg 130, Kroenke, Berger, Janecek, et al., 1991; Leg 145, Rea, Basov, Janecek, Palmer-Julson, et al., 1993). Another possible mechanism to elevate pore-water lithium (i.e., cation exchange with clays) does not appear to explain the profiles at the Ceara Rise, where the highest clay concentrations occur in lithologic Unit I, the interval in which pore-water lithium concentrations are near seawater values. We plan to investigate the possibility that the crustal cooling history at the Ceara Rise may have included a period of elevated temperatures sufficient to produce the high lithium concentrations in the pore water here, and that the lower lithium concentrations at Site 929 are explained by its position on the edge of the rise, where the crust may have cooled faster.

LOGGING CONTRIBUTIONS

The Leg 154 logging program was unusual because we were able to obtain high-quality logs at all sites. These data provide us with an opportunity to exploit downhole logs as paleoclimate tools. In addition, data from the MST natural gamma-ray sensor provide opportunities for integrating core and log data sets, as core-log depth correlations can now be established at the meter scale. The overall correspondence between core and log natural gamma-ray data sets is shown for all sites in Figure 14. Combined, the core and log data sets provide an excellent opportunity to assess the role of downhole logs as paleoclimate tools. Shipboard logging results provided evidence of profound changes in terrigenous mineralogy that occurred near 8 Ma at all sites; these changes may reflect Neogene Andean uplift and subsequent development of Amazonian drainage.

The change in mineralogy near 8 Ma was identified initially from the individual Th and K channels of the natural gamma-ray logging tool. The total natural gamma-ray log and Th/K ratio time series are shown for all sites in Figure 15. Although each site has a slightly different total gamma-ray character, a clear shift toward increased K relative to Th is seen for all sites near 8 Ma. The X-ray mineralogy of selected samples from Sites 926 and 928 (determined by XRD) demonstrate that the increased K concentrations after 8 Ma reflect an increase in illite (and quartz) relative to kaolinite and smectite in the clay mineral assemblage (Fig. 15). This mineralogic shift is coincident with a gradual increase in terrigenous MARs and may reflect the onset or intensification of granitic weathering associated with Andean uplift.

OPPORTUNITIES

Completing the drilling represents an early stage in the commitment that one makes in embarking on a paleoceanographic drilling leg. Aboard ship, documenting almost 6 km of sediment—making those measurements that can only be made on whole cores or that should be made immediately when the core is opened, and describing the core and the microfossils in it—left little time for in-depth studies or laboratory work. On board Leg 154, we did not even have time for detailed sampling, deferring that effort to the repository. However, we did have time to consider some of the opportunities presented by the material we recovered.

Biostratigraphy

The material collected during Leg 154 will serve as classic sections for investigating the evolution of the calcareous nannofossils and foraminifers. There are three reasons for this: first, the western tropical Atlantic has supported rich assemblages of these groups throughout the Cenozoic (many species were first described from land sections on the adjacent continent); second, it appears that many species evolved in this part of the ocean, so that evolutionary lineages may be traced in the Leg 154 sediments; and third, completeness of the sections recovered is documented both by hole-to-hole comparisons and by site-to-site comparisons. In addition, the pervading orbital scale lithologic cyclicity of all the sections suggests that it will be possible to develop an astronomically calibrated time scale for much of the Cenozoic at these sites. Finally, the well-documented correlation between sediments that accumulated at different water depths, but that underlie identical water masses, and thus sample the remains of the same planktonic populations, enables us to compare the effect of preservation on the observed ages of first and last appearances with a degree of rigor that is seldom attainable. The preservation of the calcareous microfossil material is exceptionally good, particularly with regard to the foraminifers. It has been a long time since such a reservoir of new material for study has been available. Excellent use of the new material was already made on board the ship, and the time is ripe for a new synthesis of low-latitude Cenozoic biostratigraphy. The well-documented completeness of the sections and the high-resolution time control that will be provided through astronomical calibration mean that these sites will provide ideal material for studying rates and processes of evolution in foraminifers and calcareous nannofossils in one of the oceanic regions that is regarded as a center of evolutionary action. The material is, of course, equally valuable for paleoecologic reconstructions.

Time-scale Calibration

The opportunities for astronomical calibration of the Cenozoic time scale are excellent despite our disappointing inability to recover material suitable for magnetostratigraphy. It is clear that the whole record is characterized by cyclic lithologic variations. With composite sections completed for every site through the last 6 m.y., it seems certain that it will be possible to verify or improve the calibrations provided by Hilgen (1991a, 1991b) and Shackleton et al. (in press). We have already shown (Fig. 8) the precision with which the five sites may be correlated and placed on a time scale using only biostratigraphic age control, and it is already evident that the records are far superior in terms of the regularity of sedimentation rate and the consistency in variability to those previously available for tuning.

With the opportunity to piece together very good records from four sites into the Oligocene, and two of them into the Eocene (in

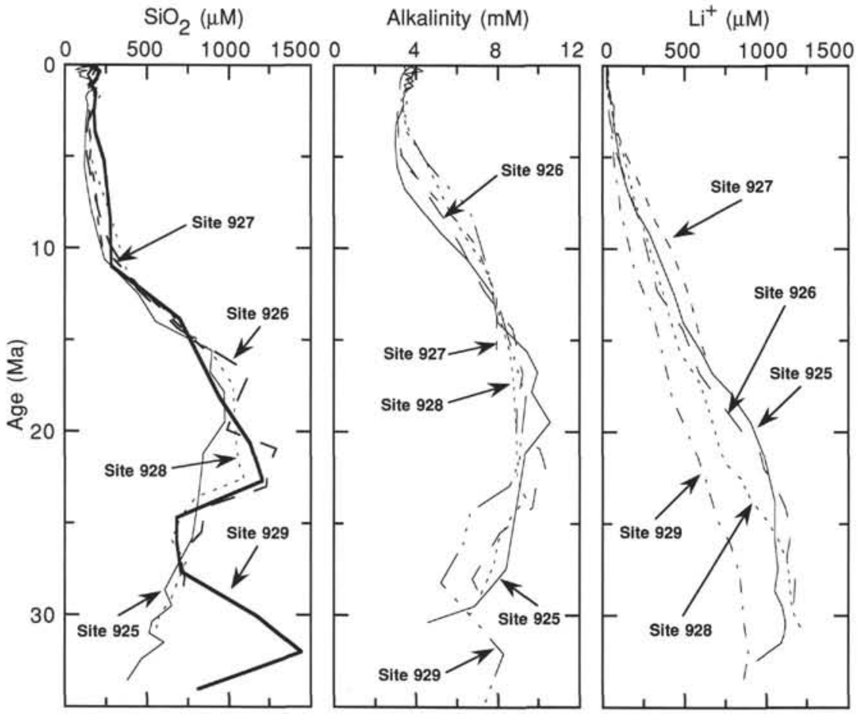

Figure 13. Silica, alkalinity, and lithium concentrations in pore waters vs. age at all sites.

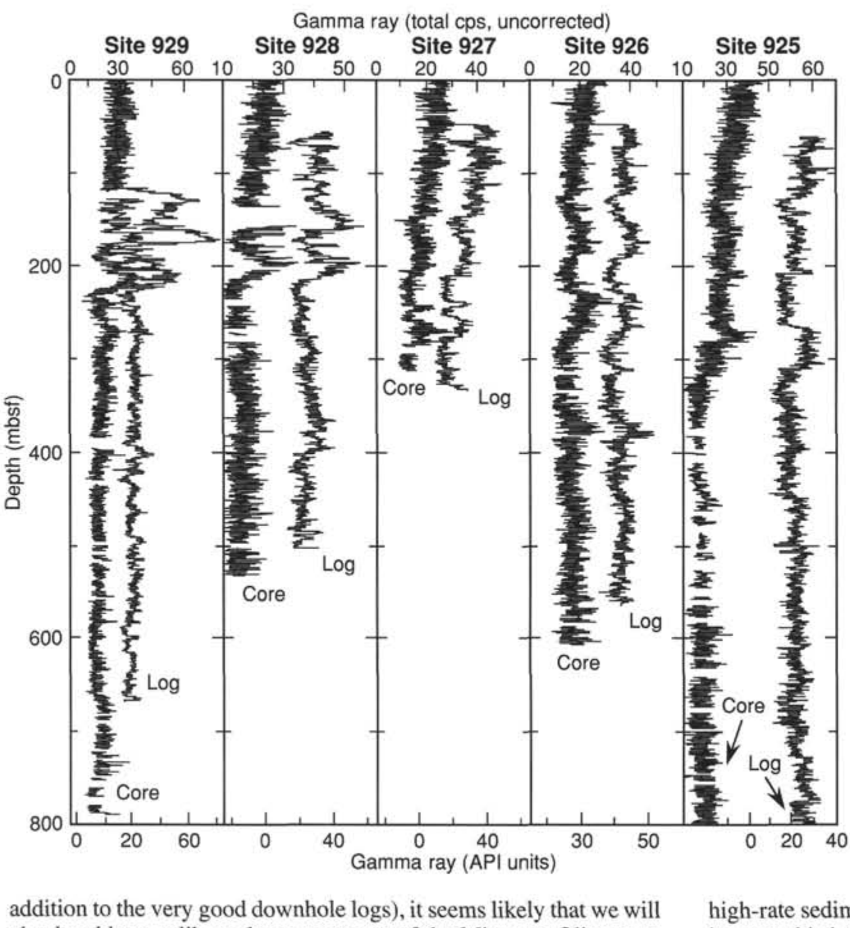

Figure 14. Downhole and core natural gamma records for Sites 925 through 929.

addition to the very good downhole logs), it seems likely that we will also be able to calibrate large segments of the Miocene, Oligocene, and Eocene. A portion of the Site 926 core reflectivity, susceptibility, and natural gamma-ray data is compared to the log natural gamma-ray and resistivity in Figure 16. A composite core section was not assembled for this interval because only one hole (926B) cored this high-rate sedimentation portion of the sequence. Lithologic variability over this interval is characterized by regular carbonate-marl bedding cycles centered at the 41-k.y. periodicity. This same mode of variability is apparent in both the log gamma ray and resistivity, and detailed correlations are possible between the core and log records. Correlations between the core and log data sets at Sites 925 and 926

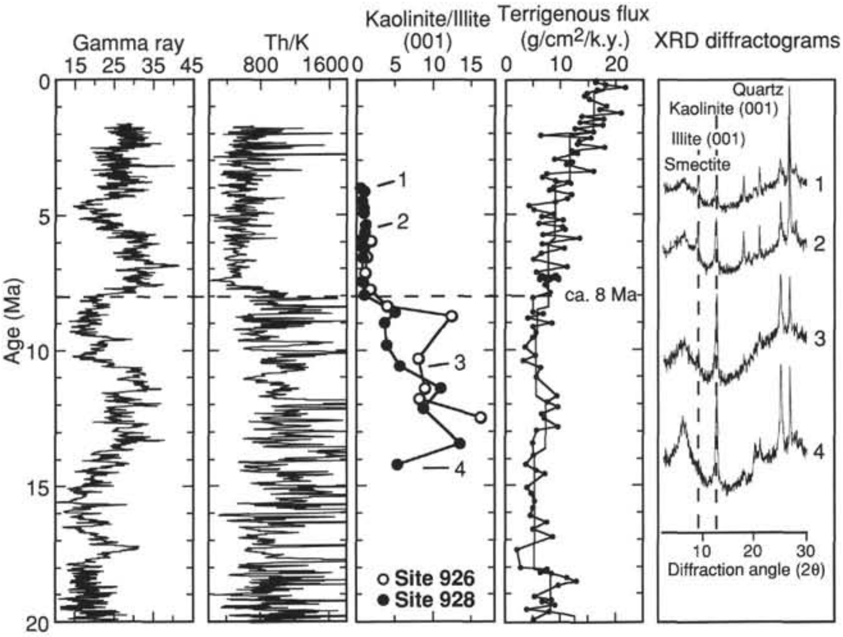

Figure 15. Log natural gamma (Site 926), Th/K ratio (Site 926), kaolinite/illite ratios from XRD (Sites 926 and 928), terrigenous flux (Site 926), and XRD diffractograms (Site 926).

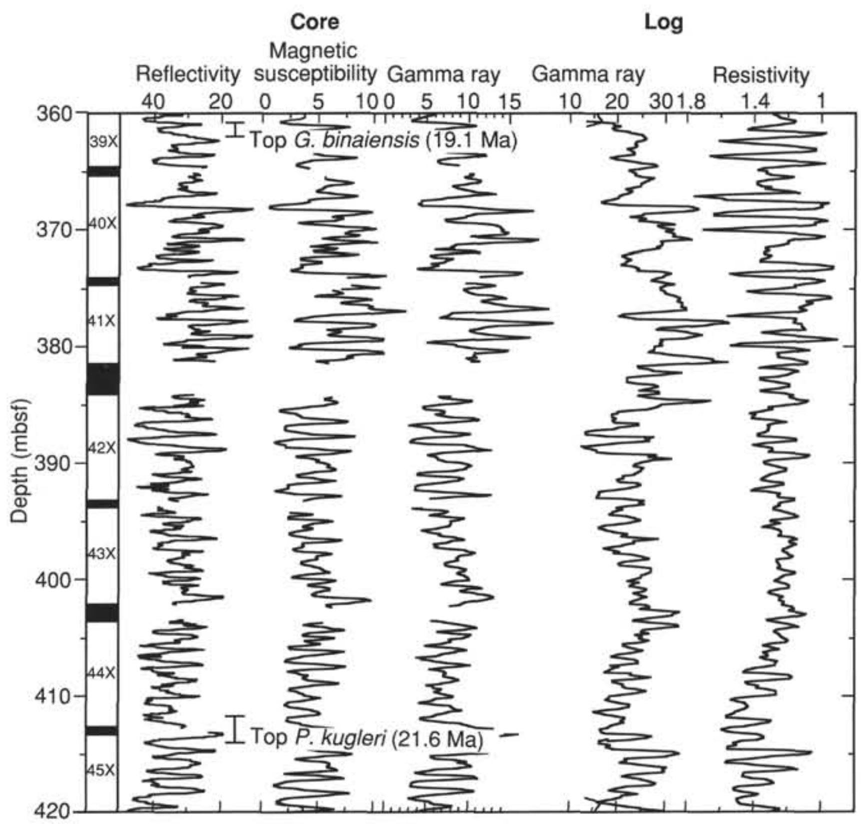

Figure 16. Core and downhole log data from Site 926. The cycles have a wavelength of about 1.5 m, which corresponds to about 40 k.y. (cf. 41-k.y. obliquity period).

can be established from roughly 19 to 33 Ma, offering an excellent opportunity to establish an orbitally tuned chronology extending into the Oligocene.

For the Pliocene and Pleistocene, astronomical calibrations can be successfully transferred to other sections using benthic oxygen isotope stratigraphy (Shackleton et al., 1990; Tiedemann et al., 1994) and/or high precision nannofossil stratigraphy (Raffi et al., 1993) for correlation. For the Miocene, bulk sediment ^{13}C stratigraphy will probably be a useful additional technique. The value of any astronomical calibrations of elapsed time that we achieve in early Miocene and Oligocene sediments will be greatly enhanced by high-precision ^{87}Sr stratigraphy, as this will permit us to transfer our calibrations to other sections that have been calibrated magnetostratigraphically.

Paleoceanography

The primary goal of Leg 154 was to provide an opportunity to reconstruct the late Neogene paleoceanography. Shipboard work has cleared the way for this endeavor to proceed immediately. Composite sections generated for all five sites enable any time interval to be selected and covered at a chosen sampling interval in time at all sites over a water depth range of 1.3 km. Fluxes of the various sedimentary components can be examined in relation to surface productivity, terrigenous input (from the Amazon) through surface and deep transport, and carbonate dissolution. Gradients in paleonutrient tracers such as ^{13}C, Cd, and Ba in foraminiferal tests may be determined. By coordinating the initial exploitation of the material available from these sites so as to minimize complications that arise from poor interlaboratory calibration, it should be possible for the first time to make confident estimates of changes in vertical benthic ^{18}O gradients. This will, of course, pave the way for making more reliable reconstructions of interoceanic gradients in deep-water properties, making use of ODP sites that have been drilled elsewhere.

The sections recovered during Leg 154 provide an excellent opportunity to determine how ocean chemistry changed in association with the growth of Antarctic glaciation. Sites 925, 926, 928, and 929 all recovered sediments coeval with the middle Oligocene increase in ^{18}O (Oi-2; Wright et al., 1992; Zachos et al., 1993), whereas Sites 925 and 928 recovered sediments coeval with the early Oligocene ^{18}O event (Oi-1). The opportunity to add to our understanding of Paleogene sedimentary budgets is also good: the shallowest and deepest members of the transect (Sites 925 and 929), separated vertically by 1300 m, both extend to the middle Eocene (Site 929 provides information into the Paleocene), and, although the Eocene sediments are moderately lithified, the biostratigraphic age control provided by the nannofossils is still very good. Benthic foraminifers appear to be sufficiently well preserved to provide valuable faunal, isotopic, and geochemical data that will help us to unravel the complexities of Eocene ocean deep-water circulation (Kennett and Stott, 1991; Miller et al, 1987b).

One attraction of the Ceara Rise as a drilling target is that it underlies a surface-water mass that is, and probably was in the past, a good example of the warmest part of the world-ocean surface. Yet, because of the significant terrigenous input through much of the Cenozoic record, the sedimentation rates are much higher than are usually observed under these low productivity waters. From a paleoclimatic standpoint, this is significant because the paleotemperature of such water masses is of great importance for modeling past atmospheric circulation, although at present it is a topic of considerable controversy. The surface chemistry of these waters is also important for modeling past atmospheric CO_2 (Broecker, 1982), for which purpose the well-preserved planktonic foraminifer tests in the sediments of the shallower Leg 154 sites will be ideal.

Finally, the terrigenous input in itself provides considerable opportunities. Shipboard work has already indicated the potential for learning more of the erosional history of the Amazon Basin. The potential for combining flux studies with chemical characterization of the terrigenous input (both inorganic and organic) offers a fascinating challenge.

REFERENCES*

Baldauf, J.G., and Barron, J.A., 1990. Evolution of biosiliceous sedimentation patterns—Eocene through Quaternary: paleoceanographic response to polar cooling. *In* Bleil, U., and Thiede, J. (Eds.), *Geological History of the Polar Oceans: Arctic Versus Antarctic:* Dordrecht (Kluwer Academic), 575–607.

Barker, P.F., Kennett, J.P., et al., 1990. *Proc. ODP, Sci. Results,* 113: College Station, TX (Ocean Drilling Program).

Barrera, E., and Huber, B.T., 1991. Paleogene and early Neogene oceanography of the southern Indian Ocean: Leg 119, foraminifer stable isotope results. *In* Barron, J., Larsen, B., et al., *Proc. ODP, Sci. Results,* 119: College Station, TX (Ocean Drilling Program), 693–717.

Barrett, P.J., Hambrey, M.J., Harwood, D.M., Pyne, A.R., and Webb, P.-N., 1989. Synthesis. *In* Barrett, P.J. (Ed.), *Antarctic Cenozoic History from the CIROS-1 Drillhole, McMurdo Sound:* DSIR Bull. N.Z., 245:241–251.

Benjamin, M., Johnson, N.M., and Naeser, C.W., 1987. Recent rapid uplift in the Bolivian Andes: evidence from fission-track dating. *Geology,* 15:680–683.

Biolzi, M., 1985. The Oligocene/Miocene boundary in selected Atlantic, Mediterranean and Paratethyan sections based on stratigraphic and stable isotope evidence [Ph.D. thesis]. Univ. Padova, Italy.

Bohrmann, G., and Stein, R., 1989. Biogenic silica at ODP Site 647 in the southern Labrador Sea: occurrence, diagenesis, and paleoceanographic implications. *In* Srivastava, S.P., Arthur, M.A., Clement, B., et al., *Proc. ODP, Sci. Results,* 105: College Station, TX (Ocean Drilling Program), 155–170.

Broecker, W.S., 1982. Glacial to interglacial changes in ocean chemistry. *Prog. Oceanogr.,* 11:151–197.

Ciesielski, P.F., Kristoffersen, Y., et al., 1988. *Proc. ODP, Init. Repts.,* 114: College Station, TX (Ocean Drilling Program).

CLIMAP Project Members, 1976. The surface of the ice-age Earth. *Science,* 191:1131–1137.

Gieskes, J.M., 1981. Deep-sea drilling interstitial water studies: implications for chemical alteration of the oceanic crust, layers I and II. *In* Warme, J.E., Douglas, R.G., and Winterer, E.L. (Eds.), *The Deep Sea Drilling Project: A Decade of Progress.* Spec. Publ.—Soc. Econ. Paleontol. Mineral., 32:149–167.

Gieskes, J.M., Elderfield, H., Lawrence, J.R., Johnson, J., Meyers, B., and Campbell, A., 1982. Geochemistry of interstitial waters and sediments, Leg 64, Gulf of California. *In* Curray, J.R., Moore, D.G., et al., *Init. Repts. DSDP,* 64 (Pt. 2): Washington (U.S. Govt. Printing Office), 675–694.

Hilgen, F.J., 1991a. Astronomical calibration of Gauss to Matuyama sapropels in the Mediterranean and implication for the geomagnetic polarity time scale. *Earth Planet. Sci. Lett.,* 104:226–244.

————, 1991b. Extension of the astronomically calibrated (polarity) time scale to the Miocene/Pliocene boundary. *Earth Planet. Sci. Lett.,* 107:349–368.

Hsü, K.J., LaBrecque, J.L., et al., 1984. *Init. Repts. DSDP,* 73: Washington (U.S. Govt. Printing Office).

Keller, G., and Barron, J.A., 1983. Paleoceanographic implications of Miocene deep-sea hiatuses. *Geol. Soc. Am. Bull.,* 97:590–613.

Kennett, J.P., and Shackleton, N.J., 1976. Oxygen isotopic evidence for the development of the psychrosphere 38 Myr ago. *Nature,* 260:513–515.

Kennett, J.P., and Stott, L.D., 1991. Abrupt deep-sea warming, paleoceanographic changes and benthic extinctions at the end of the Palaeocene. *Nature,* 353:225–229.

Kroenke, L.W., Berger, W.H., Janecek, T.R., et al., 1991. *Proc. ODP, Init. Repts.,* 130: College Station, TX (Ocean Drilling Program).

Martin, J.B., Kastner, M., and Elderfield, H., 1991. Lithium: sources in pore fluids of Peru slope sediments and implications for oceanic fluxes. *Mar. Geol.,* 102:281–292.

Mayer, L., Pisias, N., Janecek, T., et al., 1992. *Proc. ODP, Init. Repts.,* 138 (Pts. 1 and 2): College Station, TX (Ocean Drilling Program).

Miller, K.G., Fairbanks, R.G., and Mountain, G.S., 1987a. Tertiary oxygen isotope synthesis, sea-level history, and continental margin erosion. *Paleoceanography,* 2:1–19.

Miller, K.G., Janecek, T.R., Katz, M.E., and Keil, D.J., 1987b. Abyssal circulation and benthic foraminiferal changes near the Paleocene/Eocene boundary. *Paleoceanography,* 2:741–761.

Miller, K.G., Wright, J.D., and Fairbanks, R.G., 1991. Unlocking the Ice House: Oligocene-Miocene oxygen isotopes, eustasy, and margin erosion. *J. Geophys. Res.,* 96:6829–6848.

Peterson, L.C., Murray, D.W., Ehrmann, W.U., and Hempel, P., 1992. Cenozoic carbonate accumulation and compensation depth changes in the Indian Ocean. *In* Duncan, R.A., Rea, D.K., Kidd, R.B., von Rad, U., and Weissel, J.K. (Eds.), *Synthesis of Results from Scientific Drilling in the Indian Ocean.* Geophys. Monogr., Am. Geophys Union, 70:311–333.

Pisias, N.G., Mayer, L.A., Janecek, T.R., Palmer-Julson, A., and van Andel, T.H. (Eds.), in press. *Proc. ODP, Sci. Results,* 138: College Station, TX (Ocean Drilling Program).

Raffi, I., Backman, J., Rio, D., and Shackleton, N.J., 1993. Plio-Pleistocene nannofossil biostratigraphy and calibration to oxygen isotopes stratigraphies from Deep Sea Drilling Project Site 607 and Ocean Drilling Program Site 677. *Paleoceanography,* 8:387–408.

*Abbreviations for names of organizations and publications in ODP reference lists follow the style given in *Chemical Abstracts Service Source Index* (published by American Chemical Society).

Raffi, I., and Flores, J.A., in press. Pleistocene through Miocene calcareous nannofossils from eastern equatorial Pacific Ocean (Leg 138). *In* Pisias, N.G., Mayer, L.A., Janecek, T.R., Palmer-Julson, A., and van Andel, T.H. (Eds.), *Proc. ODP, Sci. Results,* 138: College Station, TX (Ocean Drilling Program).

Rea, D.K., Basov, I.A., Janecek, T.R., Palmer-Julson, A., et al., 1993. *Proc. ODP, Init. Repts.,* 145: College Station, TX (Ocean Drilling Program).

Ruddiman, W., Sarnthein, M., Baldauf, J., et al., 1988. *Proc. ODP, Init. Repts.,* 108 (Section 2): College Station, TX (Ocean Drilling Program).

Schlich, R., Wise, S.W., Jr., et al., 1989. *Proc. ODP, Init. Repts.,* 120: College Station, TX (Ocean Drilling Program).

Shackleton, N.J., Berger, A., and Peltier, W.R., 1990. An alternative astronomical calibration of the lower Pleistocene timescale based on ODP Site 677. *Trans. R. Soc. Edinburgh, Earth Sci.,* 81:251–261.

Shackleton, N.J., Crowhurst, S., Hagelberg, T., Pisias, N.G., and Schneider, D.A., in press. A new late Neogene time scale: application to Leg 138 sites. *In* Pisias, N.G., Mayer, L.A., Janecek, T.R., Palmer-Julson, A., and van Andel, T.R. (Eds.), *Proc. ODP, Sci. Results,* 138: College Station, TX (Ocean Drilling Program).

Shipboard Scientific Party, 1972. Shipboard Report Site 77. *In* Hays, J.D., et al., *Init. Repts. DSDP,* 9: Washington (U.S. Govt. Printing Office), 43–208.

Stott, L.D., Kennett, J.P., Shackleton, N.J., and Corfield, R.M., 1990. The evolution of Antarctic surface waters during the Paleogene: inferences from the stable isotopic composition of planktonic foraminifers, ODP Leg 113. *In* Barker, P.F., Kennett, J.P., et al., *Proc. ODP, Sci. Results,* 113: College Station, TX (Ocean Drilling Program), 849–863.

Tiedemann, R., Sarnthein, M., and Shackleton, N.J., 1994. Astronomical timescale for the Pliocene Atlantic $\delta^{18}O$ and dust flux records of ODP Site 659. *Paleoceanography,* 9:619–638.

Wise, S.W., Jr., Breza, J.R., Harwood, D.M., and Wei, W., 1991. Paleogene glacial history of Antarctica. *In* Muller, D.N., McKenzie, J.A., and Weissert, H. (Eds.), *Controversies in Modern Geology:* San Diego (Academic Press), 133–171.

Woodruff, F., and Savin, S.M., 1989. Miocene deepwater oceanography. *Paleoceanography,* 4:87–140.

Wright, J.D., Miller, K.G., and Fairbanks, R.G., 1992. Early and middle Miocene stable isotopes: implications for deepwater circulation and climate. *Paleoceanography,* 7:357–389.

Zachos, J.C., Breza, J., and Wise, S.W., 1992. Early Oligocene ice-sheet expansion on Antarctica: sedimentological and isotopic evidence from Kerguelen Plateau. *Geology,* 20:569–573.

Zachos, J.C., Lohmann, K.C., Walker, J.C.G., and Wise, S.W., Jr., 1993. Abrupt climate change and transient climates during the Paleogene: a marine perspective. *J. Geol.,* 101:191–213.

Ms 154IR-109